



Effect of Deformation-Induced Martensitic Transformations in a SMAW Butt Joint of the 304 Stainless Steel on its Strain Field Distributions

ANATOLIY KLOPOTOV, MIKHAIL SLOBODYAN, ALEXANDER SMIRNOV, NIKOLAY ABABKOV, NATALYA POPOVA, KIRILL KURGAN, ARTEM USTINOV, YURIY ABZAEV, and ELENA NIKONENKO

The paper reports the effect of plane tensile stresses on changes in the microstructure and phase composition in a butt joint of plates from the 304 austenitic stainless steel obtained by shielded metal arc welding. Both evolution of strain field distributions and data obtained by transmission diffraction electron microscopy are presented. The deformation-induced $\gamma \rightarrow \alpha$ transformation was observed in addition to the $\gamma \rightarrow \varepsilon$ one. High plasticity and significant strain hardening of the steel were established. For the welded steel sample, the ratio of ultimate tensile strength to the yield point reduced from 3.3 (for the as-received metal) down to 2.6. At the elastic stage, a fragmented structure was observed in the form of local macroregions, within which strain levels differed by $\pm(30\text{--}40)\text{pct}$ from the average one over the entire area of the welded sample surface. These local macroregions were a kind of deformation or elastic-plastic domains, which could include some groups of grains. The transition from the elastic strain region to the plastic one caused a change in all strain field distributions on the welded sample surface. Small local areas merged into large homogeneous regions characterized by high strain levels. The presence of the welded joint resulted in the formation of local macroregions with both lower and higher plastic strain levels on the longitudinal and transverse field distributions in speckle images than the averaged values over the entire sample surface. These macroregions was due to the inhomogeneity of residual stresses and the deformation-induced $\gamma \rightarrow \alpha \rightarrow \varepsilon$ martensitic transformations.

<https://doi.org/10.1007/s11661-021-06566-1>

© The Minerals, Metals & Materials Society and ASM International 2022

I. INTRODUCTION

STAINLESS steels have been widely applied in various industries for many decades. However, much effort is being made to optimize their chemical and phase compositions, as well as microstructures for improving functional properties.^[1–3] Some types of equipment, vessels and structures fabricated from stainless steels have complex shapes and large dimensions, so it is necessary to use bolted connections^[4–6] or welded

joints,^[7–9] including dissimilar ones,^[10–12] for their building. Recently, additive manufacturing has begun to be widely deployed.^[13–15] It should be noted that much attention is paid to shielded metal arc welding (SMAW) of stainless steels,^[16–18] despite a significant number of other mechanized and automated methods have been developed.^[19,20] The reason is the versatility and low cost of equipment, which distinguishes this method from others, even considering its low productivity.

The microstructure and properties of weld metals (WM) differ from those of base metals (BM) because of high heating and cooling rates, as well as the use of welding consumables in some cases. This results in residual stresses and distortions in the area of welded joints.^[21–23] An analysis of the experimental data on the effect of strains on the microstructure and phase composition (at the microlevel) as well as evolution of strain field distributions (at the macrolevel) enables to predict the behavior of the welded joints in a wide range of mechanical loads. Digital image correlation methods are among the most advanced ones currently applied for

ANATOLIY KLOPOTOV, NATALYA POPOVA, KIRILL KURGAN, ARTEM USTINOV, YURIY ABZAEV, ELENA NIKONENKO are with the Tomsk State University of Architecture and Building, 2, Solyanaya Square, Tomsk, Russia, 634003. MIKHAIL SLOBODYAN is with the Tomsk Scientific Center SB RAS, 10/4, Akademicheskii Prospekt, Tomsk, Russia, 634055. Contact e-mail: s.m.s@ngs.ru ALEXANDER SMIRNOV is with the Kuzbass State Technical University, 28, Vesennyya street, Kemerovo, Russia, 650026. NIKOLAY ABABKOV is with the The Federal Research Center of Coal and Coal-Chemistry SB RAS, 18, Sovetsky Avenue, Kemerovo, Russia, 650065.

Manuscript submitted July 30, 2021; accepted: November 25, 2021.

Article published online January 8, 2022

these purposes.^[24–26] At the same time, electron microscopic studies are also necessary to understand the obtained data at the microlevel.

Features of the austenitic steel welding are the following.^[7,8] Their thermal expansion coefficient is about one and a half times greater than that of carbon steels. This fact should be taken into account to minimize distortion. The low thermal and electrical conductivity of the austenitic steels causes no need for high heat input upon fusion welding, since the heat is not conducted away from a joint. Typically, filler metals (if applied) should match the BM compositions and provide a microstructure with some ferrite to avoid hot cracking. Also, sensitization of the heat affected zone (HAZ) should be prevented.

It is known that the $\gamma \rightarrow \varepsilon \rightarrow \alpha$ martensitic transformations (MT) can take place in austenitic metastable steels at the interface between a weld pool and BM upon welding.^[7,8] In this case, the γ -phase is austenite, the ε -phase is martensite with the hexagonal close-packed (HCP) crystal lattice, and the α -phase is martensite with the body-centered cubic (BCC) microstructure. These transformations of the steel microstructure affect its functional properties. As a result, welded joints are the most critical metal regions due to the presence of stress raisers, which cause the formation of cracks and other discontinuities.^[27] Therefore, knowledge about patterns of strain field distributions in the area of the welded joints under loads enables to assess strength properties of entire welded structures and predict their behavior during operation.^[28]

To date, the microstructure transformation processes in the metastable austenitic steels and changes in their mechanical properties under various loads have been reported by many authors.^[29–31] It has been found that dynamics of these processes are determined by both types and modes of plastic strains. At the same time, much attention is paid to study patterns of these changes as a function of the defect evolution in austenite and the formation of deformation-induced martensite. It should be noted that the mechanical properties of these steels are improved due to the presence of two types of martensite phases (α' with the BCC lattice and ε with the HCP one) transformed from austenite.^[32,33] These phases possess higher strengths, but the formation of α' -martensite is more preferable because of its higher thermodynamic stability (MT can occur in the $\gamma \rightarrow \varepsilon \rightarrow \alpha'$ or $\gamma \rightarrow \alpha'$ ways^[32,33]). An important characteristic for the martensitic phases is their high resistance to plastic strains.^[32] However, few research results devoted to such processes in welded joints of the metastable austenitic steels have been published till now.^[34–36]

Based on the foregoing, the purpose of these investigations has been to study the effect of plane tensile stresses on changes in the microstructure and phase composition in a SMAW butt joint of austenitic stainless steel plates. Both evolution of strain field distributions and data obtained by transmission diffraction electron microscopy were considered.

II. MATERIAL AND METHODS

Two $70 \times 15 \times 1.5$ mm plates of the 304 austenitic stainless steel were joined by SMAW (an ‘EWM Pico 160’ welding machine) across their axis using a ‘CL-II’ electrode 2.5 mm in diameter with a basic coating.^[37,38] Their chemical compositions are presented in Table I. DCEP welding current was about 60 A. As a result, the WM width was ~ 1.5 mm, the HAZ was within 2.0 mm. According to the electrode manufacturer,^[37] the ferrite phase content in the WM was 2.5 to 10.0 pct (typical is 6.1 pct) and it was highly resistant to intergranular corrosion.^[39] The welded joint had to possess the following typical characteristics: impact strength of ~ 120 J/cm², tensile strength of ~ 660 MPa, yield point of ~ 420 MPa, and elongation of 34 pct.^[37]

Tensile loads were applied to both as-received steel and welded samples using an ‘INSTRON 3386’ electromechanical testing machine at a constant rate of 0.3 mm/min.

Strains were measured with a ‘Vic-3D’ optical system, which enabled to obtain data on displacements of points on the sample surfaces under the tensile loads. Figure 1 shows a scheme of the registration of speckle images on the welded sample surface under tensile loads. The data were recorded on the basis of an extensometer installed at the studied samples from the upper clamp of the testing machine to the lower one, as well as at the sample surfaces. An image analysis of the investigated surfaces was carried out after the formation of speckle microstructures on them, *i.e.*, irregular drawing of many points on a contrasting background. Upon the test, the ‘VicSnap’ software recorded images from two cameras simultaneously. The stereo images were processed by the ‘Vic-3D’ software that calculated displacements of the surface points in three mutually perpendicular axes by applying the digital image correlation method. The output data were the X , Y , and Z coordinates for each analyzed point; the U , V , and W displacements at each point along the X , Y , and Z axes, respectively; as well as the ε_{XX} transverse (along the X axis), ε_{YY} longitudinal (along the Y one), and ε_{XY} shear strains. As a result, a data array was obtained on the displacements of the surface metal microvolumes in the three-dimensional space. The strain fields were the projections of these local surface areas.

The use of the ‘Vic-3D’ system enabled to determine levels of average strains over the entire sample area on a fixed base under the uniaxial tensile load.^[40] As a result, deformation curves were obtained in the ‘engineering stress vs. engineering strain’ ($\sigma_{\text{eng}} - \varepsilon_{\text{eng}}$) coordinates, which were calculated by the following equations:

$$\sigma_{\text{eng}} = \left(\frac{F}{S_0} \right) \quad [1]$$

$$\varepsilon_{\text{eng}} = \left(\frac{\Delta l}{l_0} \right) \quad [2]$$

where F was tensile force, S_0 was the initial cross-sectional area of the sample, Δl was its elongation, and l_0 was the initial length of the sample.

Table I. The Chemical Compositions of the 304 Stainless Steel and the ‘CL-11’ SMAW Electrode (Wt Pct)

	C	Mn	Si	Ni	Cr	Nb	S	P	Ti	Cu	Fe
Steel	0.12	≤ 2.0	≤ 0.8	9.0–11.0	17.0–19.0	—	≤ 0.02	≤ 0.035	0.6–0.8	≤ 0.30	balance
Electrode	0.10	1.8	0.53	9.8	20.8	0.99	0.011	0.02	—	—	balance

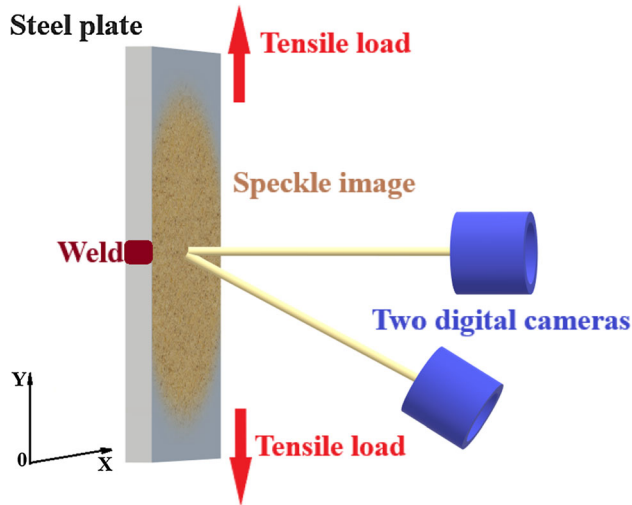


Fig. 1—The scheme of the registration of speckle images on the welded sample surface under tensile loads.

Then, the ‘engineering stress vs engineering strain’ curves were converted to the ‘true stress vs true strain’ ($\sigma_{\text{true}} - \varepsilon_{\text{true}}$) ones by the following equations^[41]:

$$\sigma_{\text{true}} = \left(\frac{F}{S_0} \right) \left(1 + \frac{\Delta l}{l_0} \right) \quad [3]$$

$$\varepsilon_{\text{true}} = \ln \left(1 + \frac{\Delta l}{l_0} \right) \quad [4]$$

The microstructure and phase composition of thin steel foils were studied by transmission electron diffraction microscopy using an ‘EM-125’ microscope with a magnification of 25,000. The foils were cut by electrical discharge machining from the BM, HAZ and WM. The following parameters of the steel microstructure were found using electron microscopic images: volume fractions of the matrix morphological components, scalar and excess dislocation densities, curvature-torsion amplitudes of the crystal lattice, as well as levels of internal stresses. Determination of sizes and volume fractions of the phases presented in the steel was carried out using images confirmed by microdiffraction patterns and dark-field ones obtained in the reflections of the corresponding phases. The phases were identified by the microdiffraction patterns calculated from the tabular values of the crystal lattice parameters of actually presented ones. The scalar dislocation density ρ was determined according to the standard technique from the micrographs by the secant method with a correction for the invisibility of dislocations.^[42] A rectangular mesh

was used as secants. The total number of intersections of dislocation lines with horizontal and vertical mesh ones was calculated.^[42] The ρ value was assessed within a single γ -phase grain.

Two types of internal stresses were determined on the basis of the electron microscopic studies.^[43] The first one was σ_{τ} shear stresses, *i.e.*, stress fields formed by the dislocation substructure (‘forest’ dislocations). The second type was σ_l long-range stresses, *i.e.*, moment (or local) stresses arising in areas with the (ρ_{\pm}) excess dislocation density:

$$\rho_{\pm} = \rho_+ - \rho_- \neq 0, \quad [5]$$

where ρ_+ and ρ_- were densities of positively and negatively charged dislocations, respectively.

Shear stresses (stress fields due to the presence of dislocations) were calculated using the formula:

$$\sigma_{\tau} = \alpha \cdot G \cdot b \cdot \sqrt{\langle \rho \rangle}, \quad [6]$$

where α were changed from 0.05 to 1.00 depending on the dislocation ensemble type^[44]; G was shear modulus, b was the Burgers vector; ρ was the scalar dislocation density.

Long-range stresses were determined from the presence of the ρ_{\pm} excess dislocation density according to the relationship:

$$\sigma_l = \alpha_C G b \sqrt{\rho_{\pm}}, \quad [7]$$

where $\alpha_C = 1$ was the Strunin coefficient.^[45]

The ρ_{\pm} excess dislocation density was found experimentally from the relationship^[46]:

$$\rho_{\pm} = \chi/b, \quad [8]$$

where χ was the average value of the curvature-torsion amplitude for the matrix crystal lattice, determined by the presence of bending extinction contours in the material, which defined as^[46]:

$$\chi = \partial\varphi/\partial l, \quad [9]$$

where φ was the goniometer-controlled tilt angle of the foil in the electron microscope column, l was the extinction contour width determined experimentally.^[46]

Moment stresses were identified by the presence of bending extinction contours in the steel.^[46] In this case, long-range stresses can be represented from the expression (7) as:

$$\sigma_l = G \sqrt{b/\chi}. \quad [10]$$

This process was based on the $\gamma \rightarrow$ twins $\rightarrow \varepsilon \rightarrow \alpha$ complex MT sequence. In the studied case, there were

mechanical (strain) microtwins based on the austenitic γ -phase with the FCC crystal lattice, as well as the HCP ε - and BCC α -phases (ε - and α -martensite, respectively).

The studied material belonged to austenitic steels, in which, austenite (the FCC γ -phase), as a rule, transforms into martensite upon deformation or/and heating.^[47–49] As a result, two microstructure types could be formed: HCP ε - and BCC α -martensite. Both processes were diffusionless in the following sequence^[47–49]: $\gamma \rightarrow$ twins $\rightarrow \varepsilon \rightarrow \alpha$, where twins could be mechanical (or strain) microtwins with the FCC crystal lattice, which parameter was equal to that of the γ -phase (austenite).

It is known^[50] that both microtwins and ε -martensite were flat plates (parallel to each other) of regular geometric shapes with clear boundaries. The habit (or twinning) plane of microtwins was the $\{111\}$ ones of austenite. Plates of ε -martensite were also formed on the $\{111\}$ ones of austenite because these close-packed planes and the (0001) plane of ε -martensite were parallel to each other, as well as the close-packed $\langle 110 \rangle_\gamma$ and $\langle 1120 \rangle_\varepsilon$ directions coincided in these planes.^[47] Due to these reasons, it was difficult to distinguish ε -martensite plates from microtwins in the direct transmission electron microscopic (TEM) study of the austenitic steel microstructures. Therefore, the steel phase composition was assessed by indication of microelectron diffraction patterns (in the presence of ε -martensite and microtwins in austenite) using a technique based on the matrix equations.^[50]

III. RESULTS AND DISCUSSION

A. Transmission Electron Microscopy

1. The as-received base metal

The results of the TEM studies showed that the as-received steel matrix was the γ -phase (austenite), *i.e.*, the FCC γ -Fe solid solution (both interstitial and substitutional). In this case, the interstitial element was carbon, while the substitutional ones were nickel, chromium, molybdenum, manganese, titanium, silicon, etc. Some of the alloying elements could be located at defects of the crystal lattice. According to Reference 47, plastic strains in austenitic steels could cause changes in their microstructure and phase composition.

The as-received steel contained γ -phase grains (austenite) with different defect structures. The first type included ones with a reticulated dislocation substructure. The second type consisted of grains, in which (along with the dislocation substructure) mechanical (or strain) microtwins were present in the form of packets of one, two, and three systems. Volume fractions of the γ -phase grains were in the following portions: austenite grains without mechanical microtwins were approximately 10 vol pct, but grains with packets of the one, two and three systems of microtwins were about 25, 40 and 15 vol pct, respectively. Their typical TEM images are shown in Figures 2, 3 and 4. All evidence is presented in these figures, namely: (1) the directions of microtwins in the γ -matrix indices; (2) a trace of the $\{111\}_\gamma$ habit plane with the indicated plane sign; (3)

microdiffraction patterns obtained from a section of the γ -phase grain containing microtwins; (4) the indicated diagrams of the microdiffraction patterns; and (5) the theoretically calculated parallelism of the planes and directions in the crystal lattices of the γ -matrix as well as microtwins are indicated for comparison with the experimentally obtained microdiffraction patterns.

Also, the results of the TEM studies of the steel microstructure showed that it was characterized by dense dislocation meshes in all grains with a rather high level of the scalar dislocation density ($\langle \rho \rangle$ was about $2.0 \times 10^{10} \text{ cm}^{-2}$). The highest dislocation density of $\sim 2.35 \times 10^{10} \text{ cm}^{-2}$ was found in grains without microtwins. The presence of microtwins contributed to a decrease in the $\langle \rho \rangle$ values down to $1.47 \times 10^{10} \text{ cm}^{-2}$ and relaxation of internal stresses.^[51] Polarization of the dislocation microstructure was in the γ -phase grains. This was evidenced by the presence of bending extinction contours inside them (Figures 2, 3 and 4). The average ρ_\pm excess dislocation density, determined on the basis of width of the bending extinction contours, was $1.97 \times 10^{10} \text{ cm}^{-2}$ that was comparable to the $\langle \rho \rangle$ value.

2. The deformed base metal

The steel deformed up to $\varepsilon_{\text{eng}} = 5$ pct was characterized by the same microstructure and phase composition as the as-received metal. Enhancing strains up to $\varepsilon_{\text{eng}} = 37$ pct caused great changes. In this case, the microstructure included γ -phase grains (up to ~ 80 vol pct) consisted of both packets of microtwins and ε -martensite plates (Figure 5). There were γ -phase grains with packets of microtwins of the same system in an amount of ~ 5 vol pct, as well as 15 vol pct ε -martensite grains (Figure 6). These data indicated that strains up to 37 pct resulted in the crystal lattice rearrangement, *i.e.*, the $\gamma \rightarrow \alpha$ transformation. The average ρ_α scalar dislocation density was $2.21 \times 10^{10} \text{ cm}^{-2}$ in α -martensite grains, which was almost 1.5 times less than the mean ρ_γ value of $3.96 \times 10^{10} \text{ cm}^{-2}$. Nevertheless, the average σ_1 local stresses were about 535 MPa in α -martensite grains. Their σ_1^{plast} plastic component was ~ 295 MPa and the σ_1^{elast} elastic one was ~ 240 MPa. Consequently, the strain effect was different for austenite and martensite grains. The elastic-plastic bending-torsion had occurred in the α -martensite crystal lattice, while only plastic bending-torsion of the crystal lattice was observed in austenite grains (σ_1 was 340 MPa, but σ_τ was 400 MPa).

After strain up to $\varepsilon_{\text{eng}} = 25$ pct, the WM microstructure mainly consisted of three types of the γ -phase grains. The first type was represented by ones with the meshed dislocation substructure. Grains of the second type contained packets of microtwins, and ones of the third type included lamellar precipitates of ε -martensite. Their typical TEM images are shown in Figures 7, 8 and 9. The fraction of grains with the meshed dislocation substructure was about 10 vol pct, the scalar dislocation density had increased up to $5.52 \times 10^{10} \text{ cm}^{-2}$. The proportion of grains with microtwins was 65 vol pct. The dislocation substructure in these grains was fragmentary, as after strain up to $\varepsilon_{\text{eng}} = 5$ pct. The scalar dislocation density was $3.38 \times 10^{10} \text{ cm}^{-2}$, while the ρ_\pm

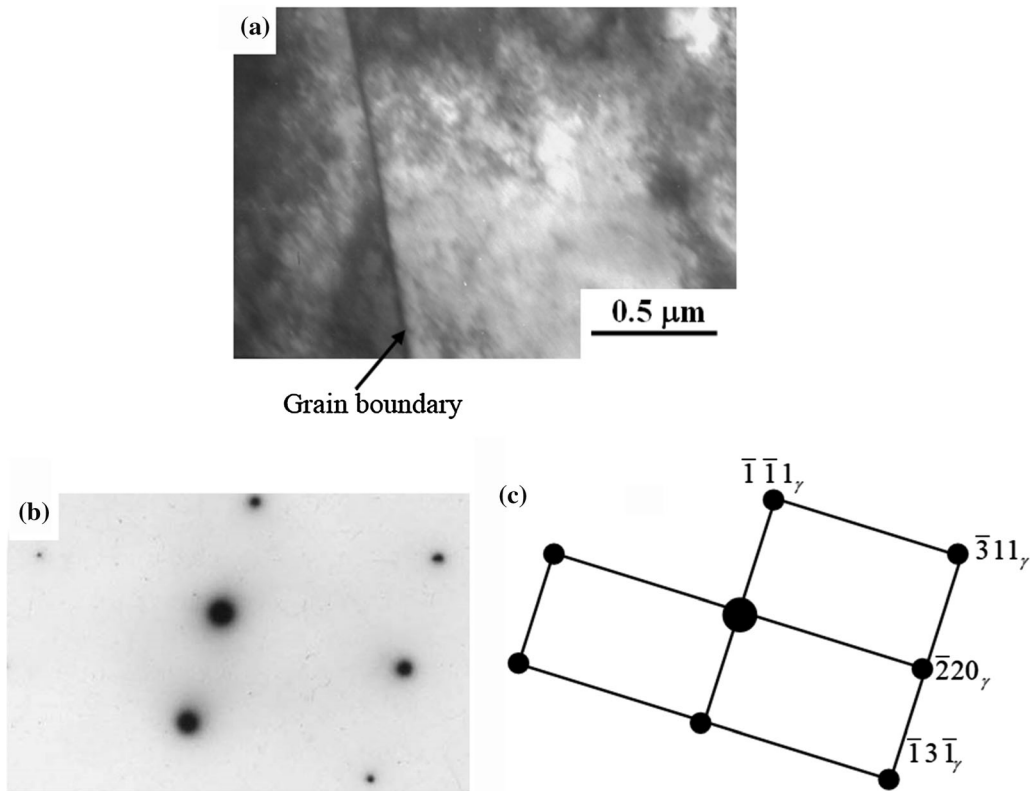


Fig. 2—TEM images of an austenite grain in the meshed substructure: (a)—bright-field image; (b)—microdiffraction pattern of the (a) area; (c)—the indicated diagram (containing reflections that belong to the (112) plane of the γ -phase).

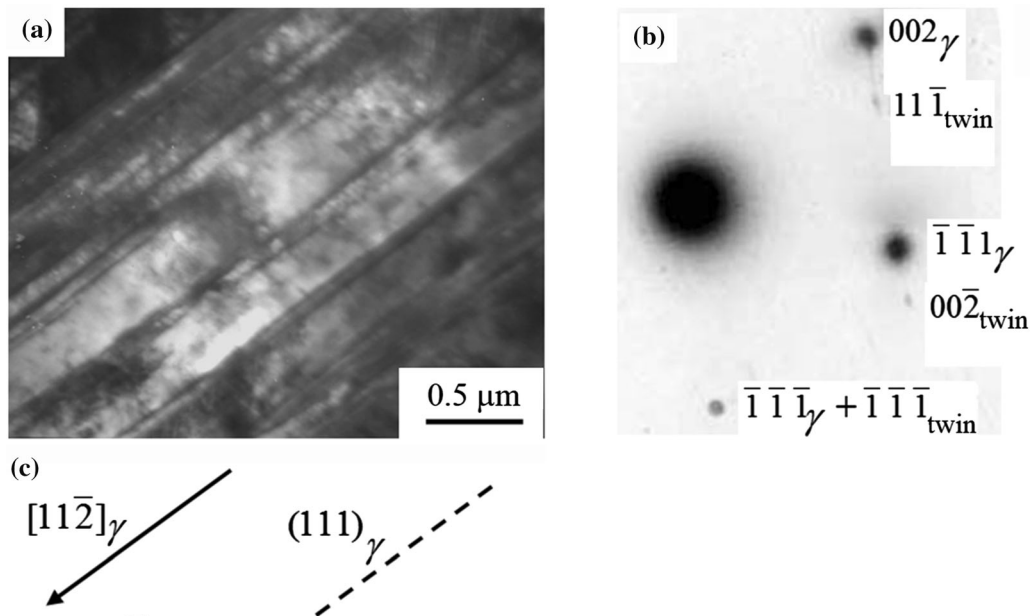


Fig. 3—TEM images of an austenite grain included a system of strain twins: (a)—bright-field image; (b)—microdiffraction pattern of the (a) area; (c)—the indicated diagram (containing reflections that belong to the $(\bar{1}10)$ plane of the γ -phase and the $(\bar{1}10)$ package of microtwins). The conditions for parallelism of the planes and the directions between the crystal lattices of the γ -matrix and the package of microtwins are satisfied: $(\bar{1}10)_\gamma \parallel (\bar{1}10)_{\text{twin}}$ and $[111]_\gamma \parallel [111]_{\text{twin}}$, the habit (twinning) plane is $(111)_\gamma$.

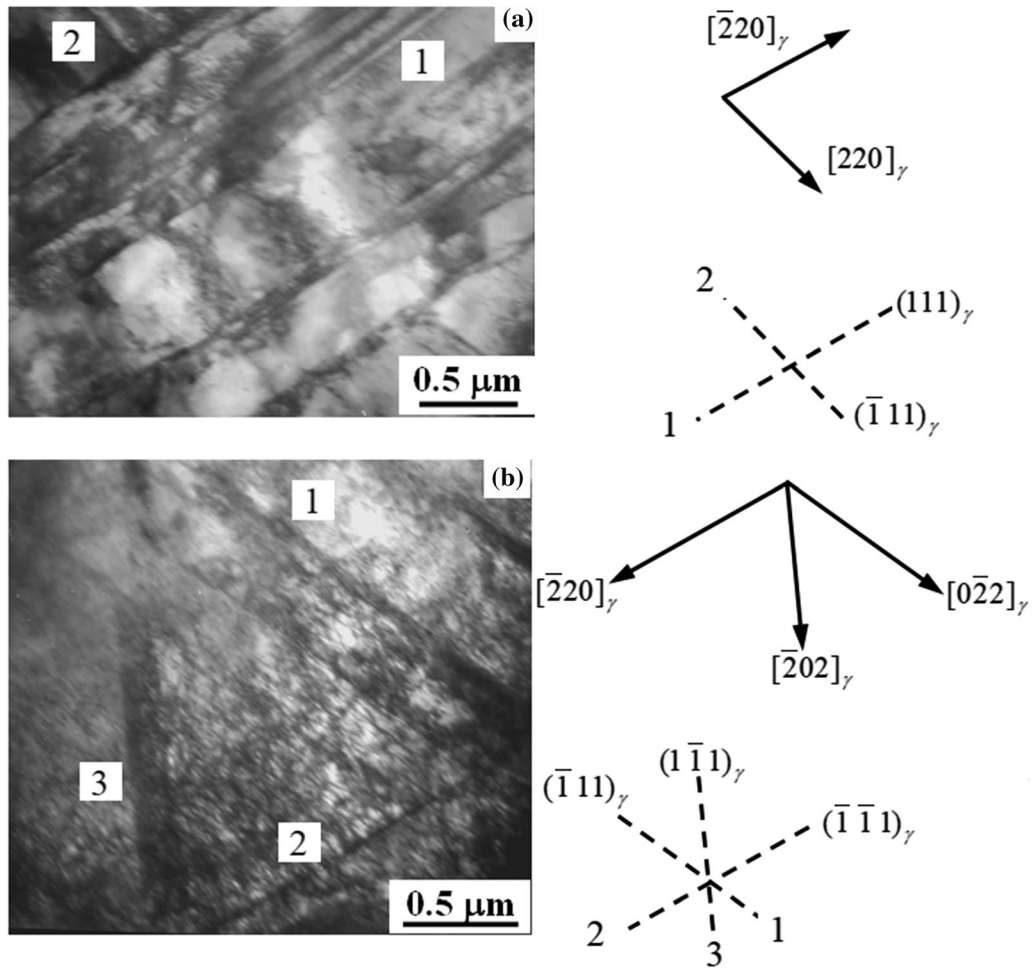


Fig. 4—TEM images of austenite grains included two (a) and three (b) systems of microtwins. The conditions for parallelism of the planes and the directions between the crystal lattices of the γ -matrix and the package of microtwins are satisfied: (a), system 1— $(001)_{\gamma} \parallel (22\bar{1})_{\text{twin}}$ and $[\bar{2}20]_{\gamma} \parallel [220]_{\text{twin}}$, the habit (twinning) plane is $(111)_{\gamma}$; (a), system 2— $(001)_{\gamma} \parallel (2\bar{2}\bar{1})_{\text{twin}}$ and $[\bar{2}20]_{\gamma} \parallel [220]_{\text{twin}}$, the habit (twinning) plane is $(1\bar{1}1)_{\gamma}$; (b), system 1— $(111)_{\gamma} \parallel (5\bar{1}1)_{\text{twin}}$ and $[022]_{\gamma} \parallel [022]_{\text{twin}}$, the habit (twinning) plane is $(111)_{\gamma}$; (b), system 2— $(111)_{\gamma} \parallel (\bar{1}\bar{1}\bar{5})_{\text{twin}}$ and $[\bar{2}20]_{\gamma} \parallel [220]_{\text{twin}}$, the habit (twinning) plane is $(111)_{\gamma}$; (b) system 3— $(111)_{\gamma} \parallel (\bar{1}\bar{5})_{\text{twin}}$ and $[202]_{\gamma} \parallel [202]_{\text{twin}}$, the habit (twinning) plane is $(111)_{\gamma}$. In the diagrams, the arrows show the directions of packets of microtwins in the γ -matrix indices, the dashed lines show the traces of the $\{111\}_{\gamma}$ habit planes.

excess dislocation density was about $4.40 \times 10^{10} \text{ cm}^{-2}$ (Table II).

The proportion of grains containing ε -martensite had increased up to 25 vol pct. It should be noted that ε -martensite of two types was in the BM microstructure after strain up to $\varepsilon_{\text{eng}} = 25$ pct. The first one included packets of parallel plates (similar to those of microtwins) located across all (or almost all) γ -phase grains (Figure 8). The second type contained short needle-shaped plates parallel to each other within a grain (Figure 9). The fraction of γ -phase grains containing plates of ε -martensite of the first type was about 5 vol pct, while the second type was near 20 vol pct. The dislocation substructure of grains containing ε -martensite of both types was represented by dense dislocation meshes, as after strain up to $\varepsilon_{\text{eng}} = 5$ pct. The average scalar dislocation density in these γ -phase grains was $4.12 \times 10^{10} \text{ cm}^{-2}$ and $4.41 \times 10^{10} \text{ cm}^{-2}$, respectively.

As in the previous case, the dislocation substructure was polarized in all γ -phase grains. The ρ_{\pm} excess dislocation densities, measured from width of the extinction contours, were determined in grains of different types. The results of these calculations are shown in Table II. It follows from these data that both $\rho > \rho_{\pm}$ and $\sigma_{\tau} > \sigma_1$ conditions were satisfied in all γ -phase grains, except in ones with microtwins. Accordingly, the bending-torsion of the γ -phase crystal lattice had been of the plastic type. In ones with microtwins, both $\rho < \rho_{\pm}$ and $\sigma_{\tau} < \sigma_1$ conditions were satisfied and, respectively, the bending-torsion of the γ -phase crystal lattice had been of the elastic-plastic type. This ratio of internal stresses had contributed to the formation of microcracks in these areas. However, they typically did not transform into macrocracks since the proportion of γ -phase grains with microtwins was not high.

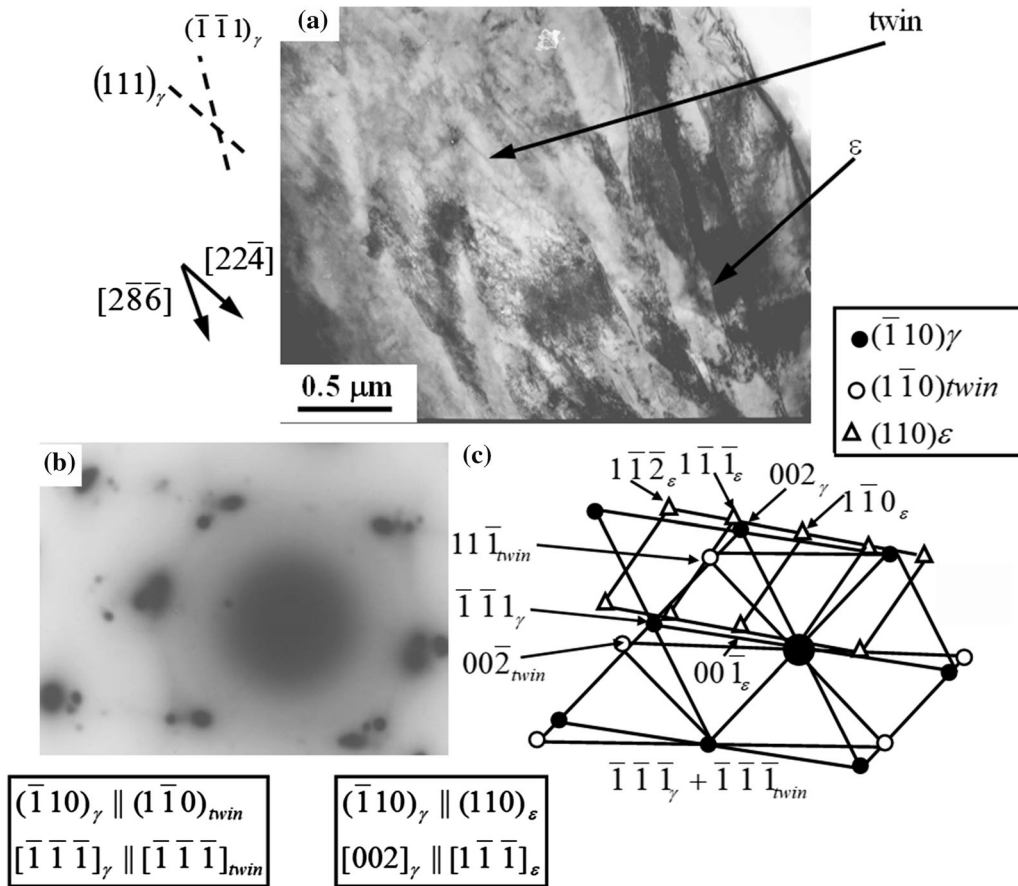


Fig. 5—TEM images of austenite grains in the steel deformed up to 37 pct. The grains contain packets of microtwins and ϵ -martensite plates: (a)—bright-field image; (b)—microdiffraction pattern; (c)—its indicated diagram. The arrows mark the directions of segregation of microtwins and ϵ -martensite plates relative to the matrix planes. The dashed lines indicate the traces of the habit planes: (111) for microtwins and $(\bar{1}\bar{1}\bar{1})$ for ϵ -martensite plates.

3. The weld metal

As expected, the microstructure and phase composition in the WM differed from those for the as-received steel. The main variations were the following. Firstly, the WM was dendritic and included γ -phase grains with only two developed systems of microtwins (Figure 10); their fraction was up to 30 vol pct. Secondly, the fraction of the γ -phase grains with ϵ -martensite packets was about 10 vol pct (Figure 11). Thirdly, γ -phase austenite grains were observed, which contained both microtwins and ϵ -martensite plates (Figure 12). Microtwins were in the form of long lamellar precipitates, while ϵ -martensite was as packets of short wide ones. In Figure 12, the theoretically calculated parallelism of the planes and the directions in the crystal lattices of the γ -phase matrix, microtwins, and ϵ -martensite plates are indicated for comparison with the obtained microdiffraction pattern. The volume fraction of such grains was 50 pct. Last but not least, it was found that the $\gamma \rightarrow \epsilon$ transformation had taken place in about half the WM volume.

The dislocation microstructure of the WM grains was in the meshed form but was polarized in the γ -phase ones. The scalar dislocation density ($\rho \sim 2.28 \times 10^{10} \text{ cm}^{-2}$) was comparable to that for the BM. The

excess dislocation density caused internal stress fields. The average σ_τ value was 300 MPa, and the σ_1 level was about 280 MPa.

4. The deformed weld metal

After plastic strain of WM up to $\epsilon_{\text{eng}} = 5$ pct, the following main changes in the microstructure and phase composition were observed. There were no γ -phase grains containing only packages of microtwins (grains of the first type). It was observed up to 30 vol pct of the second type γ -phase grains included packets of ϵ -martensite plates as well as up to 70 vol pct of the third-type ones simultaneously contained intersecting packets of microtwins and ϵ -martensite. Typical TEM images of the mentioned grains are shown in Figures 13 and 14.

An important feature should be noted. Initially, ϵ -martensite plates had been wide in the BM. In the HAZ, they had located from γ -phase grain boundaries to their central volumes. After strain up to $\epsilon_{\text{eng}} = 5$ pct, the mean width of

ϵ -martensite plates was comparable with that of microtwins, and they located from one grain boundary to the opposite. This indicated that plastic strain caused the further and more intense $\gamma \rightarrow \epsilon$ transformation in

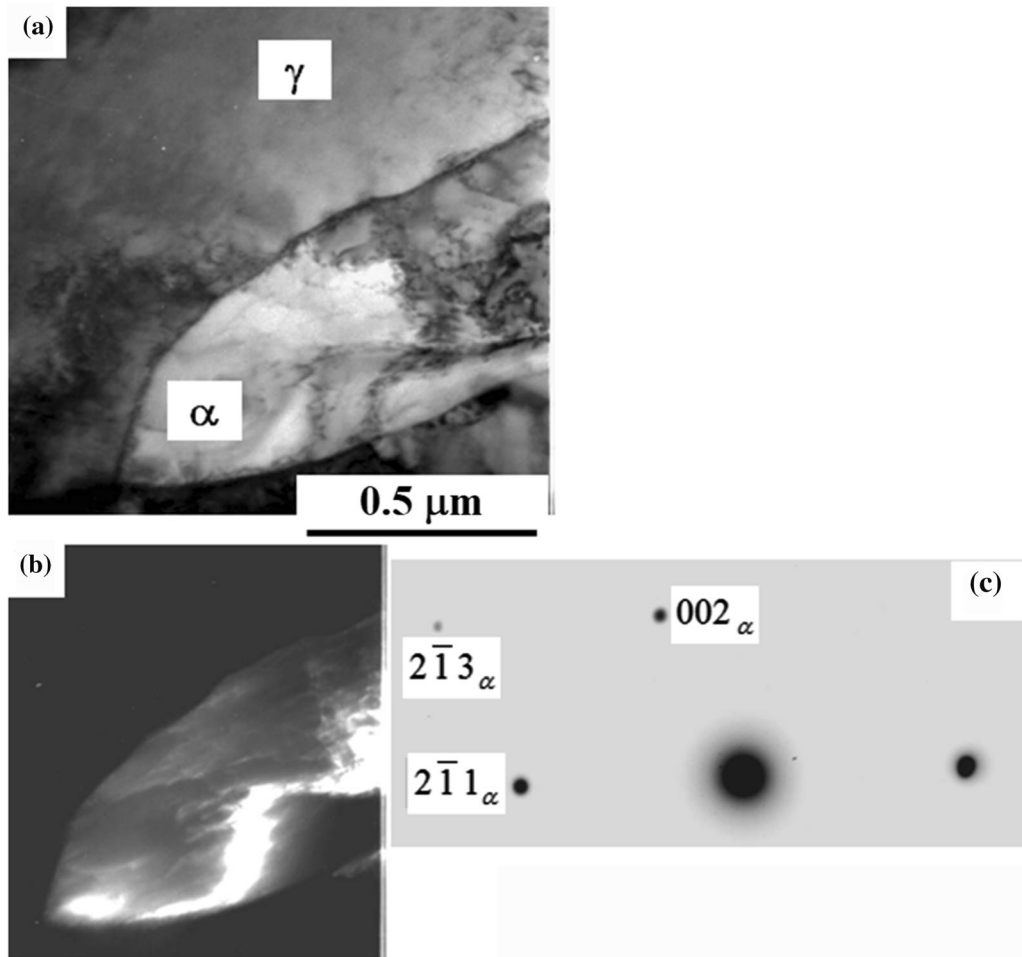


Fig. 6—TEM images of an austenite grain included an α -martensite subgrain in the steel deformed up to 37 pct: (a)—bright-field image; (b)—dark-field image obtained in the [211] reflex of the α -phase; (c)—indicated microdiffraction pattern obtained from the α -martensite subgrain (contains reflections belonging to the (120) plane of α -martensite).

austenite grains containing only ε -martensite plates (grains of the second type). The same process had been occurred in grains of the third type.

Strain up to 5 pct almost did not change the dislocation structure. In all austenite grains, it had the form of dense dislocation meshes. The scalar dislocation density slightly increased up to $3.5 \times 10^{10} \text{ cm}^{-2}$ both in grains of all types and in the WM volume. It should be noted that the ρ values differed little in grains of the second ($3.2 \times 10^{10} \text{ cm}^{-2}$) and third ($3.6 \times 10^{10} \text{ cm}^{-2}$) types.

Plastic strains also had caused a more intense polarization of the dislocation structure in the γ -phase grains. However, the excess dislocation density had increased insignificantly. The mean ρ_{\pm} value was $2.28 \times 10^{10} \text{ cm}^{-2}$ for all grain types. The mean σ_{τ} value was 375 MPa and σ_1 was about 300 MPa. The $\sigma_{\tau} > \sigma_1$ condition was fulfilled in all WM and HAZ grains. It was concluded on this basis that the crystal lattice had been subjected only to plastic strains.

After strain up to $\varepsilon_{\text{eng}} = 25$ pct, the WM microstructure represented only by γ -phase grains with mechanical microtwins and ε -martensite plates. The scalar

dislocation density was $6.18 \times 10^{10} \text{ cm}^{-2}$ and the excess dislocation density was $3.40 \times 10^{10} \text{ cm}^{-2}$, while internal stresses were $\sigma_1 = 500$ MPa and $\sigma_{\tau} = 370$ MPa, respectively. Thus, $\rho > \rho_{\pm}$ and $\sigma_1 > \sigma_{\tau}$ conditions were fulfilled in all γ -phase grains. Accordingly, bending-torsion of the γ -phase crystal lattice had a plastic character.

Strain up to $\varepsilon_{\text{eng}} = 37$ pct had caused significant changes in the microstructure and phase composition of the WM. The main one had been the formation of the BCC α -martensite grains under high external stresses. Their proportion was about 20 vol pct. Typical TEM images of the WM microstructure are shown in Figure 15. α -Martensite was both in the form of individual grains (Figure 15(a)) and their groups (Figure 15(b)). The average α -martensite grain size was $\sim 1.5 \mu\text{m}$.

In addition, intense fragmentation of the dislocation substructure had occurred in austenite grains. The average size of dislocation fragments was ~ 400 nm. Despite this fragmentation, the scalar dislocation density had increased in the γ -phase grains. As after strain up to $\varepsilon_{\text{eng}} = 5$ pct, the ρ values differed little in γ -phase grains of various types (ρ was $3.8 \times 10^{10} \text{ cm}^{-2}$ in the

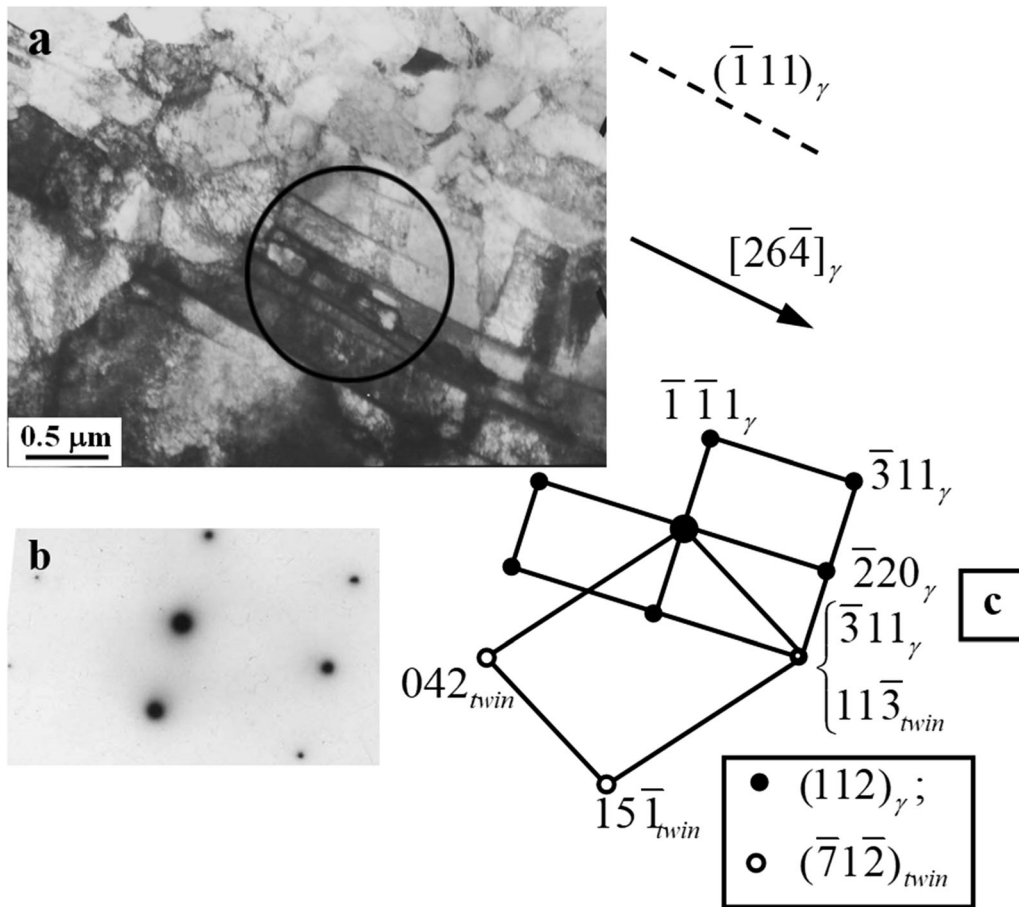


Fig. 7—TEM images of an austenite grain contained packets of microtwins in the weld metal deformed up to 25 pct: (a)—bright-field image; (b)—microdiffraction pattern obtained from the area marked with a circle in (a); (c)—the indicated scheme (there are reflexes belonging to the γ -phase and microtwins planes). Above (a), the dashed line shows a trace of the $(111)_\gamma$ habit plane; the arrow presents the segregation direction of microtwins in the γ -matrix indexes. The conditions for parallelism of the planes and the directions between the γ -matrix and microtwins are satisfied: $(112)_\gamma \parallel (712)_{twin}$ and $[\bar{3}11]_\gamma \parallel [11\bar{3}]_{twin}$.

second-type grains and it was $4.0 \times 10^{10} \text{ cm}^{-2}$ in the third-type ones). The average ρ dislocation density value was $3.8 \times 10^{10} \text{ cm}^{-2}$ in the γ -phase grains and it was $1.6 \times 10^{10} \text{ cm}^{-2}$ in α -martensite ones (more than two times less). The integral average scalar dislocation density slightly decreased down to $3.4 \times 10^{10} \text{ cm}^{-2}$.

Polarization of the dislocation substructure had also increased in all γ -phase grains. The average value of the excess dislocation density was $2.74 \times 10^{10} \text{ cm}^{-2}$, and both types of the grains were characterized by almost the same ρ_\pm levels. The mean σ_τ value was 390 MPa, σ_1 was about 325 MPa (they were almost the same in all γ -phase grains). The $\sigma_\tau > \sigma_1$ condition was fulfilled in all WM γ -phase grains. This meant that the crystal lattice had been only plastically deformed, as in the previous cases.

The dislocation substructure was polarized in both α - and γ -phase grains. However, the ρ_\pm excess dislocation density value was higher in the α -phase than that of the ρ scalar one. Since the $\rho < \rho_\pm$ condition was fulfilled, the bending-torsion of the α -phase crystal lattice had been of the elastic-plastic type. The mean σ_τ value was 255 MPa, σ_1 was about 300 MPa (the plastic component was 255 MPa and the elastic one was 45 MPa). Thus,

the $\sigma_\tau < \sigma_1$ condition was fulfilled in the α -phase, although the σ_1 value slightly exceeded the σ_τ one. Nevertheless, this meant that the presence of the α -martensite grains could cause the formation of microcracks in these areas of welded joints.

The conditions for parallelism of the planes and the directions between the γ -matrix and the (ϵ_1 and ϵ_2) packets of ϵ -martensite plates are satisfied: $(112)_\gamma \parallel (431)_{\epsilon_1}$, $[\bar{3}\bar{1}\bar{1}]_\gamma \parallel [\bar{1}\bar{2}\bar{2}]_{\epsilon_1}$, $(112)_\gamma \parallel (311)_{\epsilon_2}$ and $[2\bar{2}0]_\gamma \parallel [\bar{1}21]_{\epsilon_2}$.

Thus, the results of the TEM studies showed that strains had caused the martensitic transformation (both in BM and WM) in the following sequence: $\gamma \rightarrow \text{twins} \rightarrow \epsilon \rightarrow \alpha$, where twins could be mechanical (or strain) microtwins with the FCC crystal lattice, which parameter was equal to that of the γ -phase (austenite). These results were in good agreement with the published data.^[43,49]

B. Mechanical Tests

In the process of uniaxial tension of the samples, engineering stress-strain curves were plotted in the

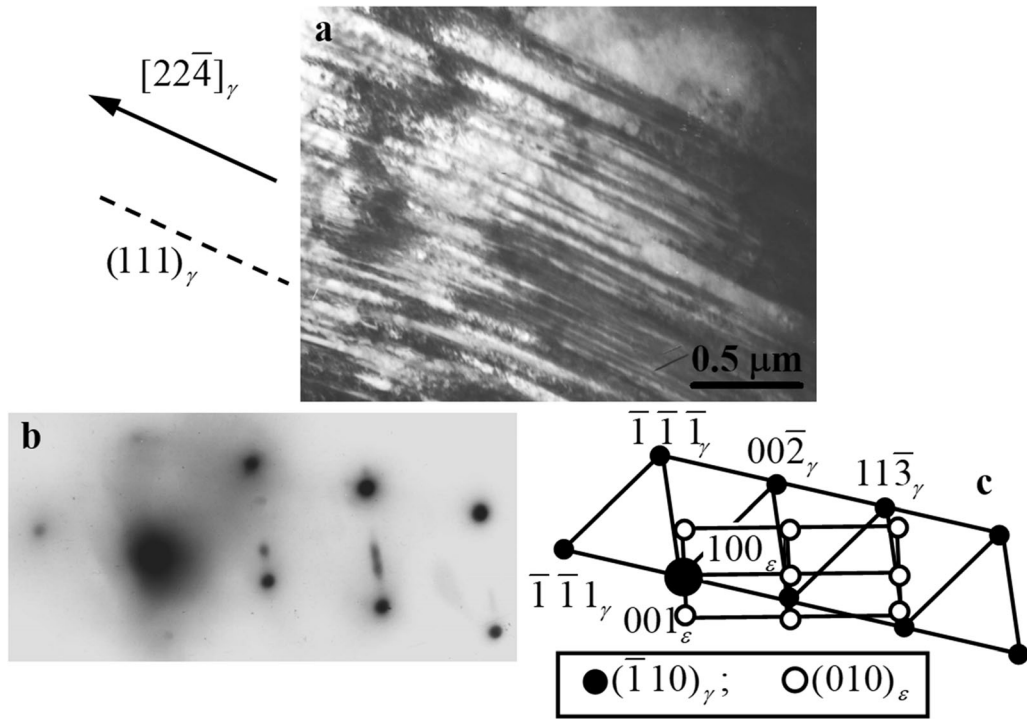


Fig. 8—TEM images of an austenite grain containing both packets of microtwins and ϵ -martensite plates in the weld metal deformed up to 25 pct: (a)—bright-field image; (b)—microdiffraction pattern obtained from (a); (c)—the indicated scheme (there are reflexes belonging to the γ -phase and ϵ -martensite plates). Near (a), the dashed line indicates the trace of the $(111)_\gamma$ habit plane; the arrow shows the segregation direction of ϵ -martensite in the γ -matrix indexes. The conditions for parallelism of the planes and the directions between the γ -matrix and ϵ -martensite are satisfied: $(\bar{1}10)_\gamma \parallel (010)_\epsilon$ and $[111]_\gamma \parallel [001]_\epsilon$.

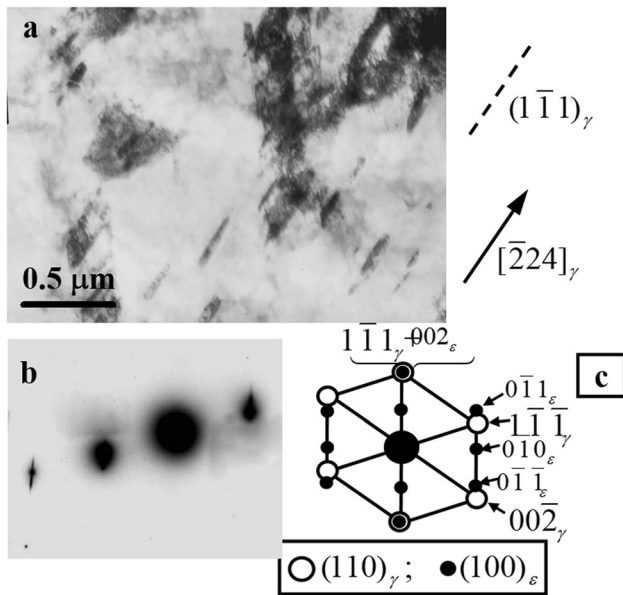


Fig. 9—TEM images of an austenite grain containing needle-shaped ϵ -martensite plates in the weld metal deformed up to 25 pct: (a)—bright-field image; (b)—microdiffraction pattern obtained from (a); (c)—the indicated scheme (there are reflexes belonging to the γ -phase and ϵ -martensite plates). Near (a), the dashed line indicates the trace of the $(111)_\gamma$ habit plane; the arrow shows the segregation direction of ϵ -martensite in the γ -matrix indexes. The conditions for parallelism of the planes and the directions between the γ -matrix and ϵ -martensite are satisfied: $(110)_\gamma \parallel (010)_\epsilon$ and $[1\bar{1}1]_\gamma \parallel [001]_\epsilon$.

$\sigma_{\text{eng}}-\epsilon_{\text{eng}}$ coordinates (Figure 16(a)). The one obtained for the as-received steel sample was similar to the data published by other authors.^[52] The as-received steel was characterized by relatively high plasticity and significant strain hardening, since the ultimate tensile strength value was 2.0 to 2.5 times higher than the yield point level (Figure 16(a), curve A). The dynamics of the welded sample deformation was also characteristic of similar cases because the ratio between these parameters significantly decreased (Figure 16(a), curve B).

According to the technique described in Section 2, the ‘true stress–true strain’ curves were also drawn in the $\sigma_{\text{true}}-\epsilon_{\text{true}}$ coordinates (Figure 16(b)). Considering the change in the cross-sectional area of the as-received steel sample under uniaxial tension, curve A in Figure 16(b) shows that its ultimate tensile strength was 3.3 times higher than the yield point value. The presence of the welded joint was also well manifested in the second case (Figure 16(b), curve B). For this sample, the ratio of ultimate tensile strength to the yield point decreased down to 2.6. The analysis of the presented curves enabled to draw a conclusion that failure of both samples had occurred at the same plastic strain levels, but at various ultimate tensile strength values. This fact reflected the presence of the joint and the ongoing changes in the microstructure and phase composition in the weld region, described above.

On both curves in the $\sigma_{\text{true}}-\epsilon_{\text{true}}$ coordinates, a decrease in the cross-section promoted an increase in effective stresses by the $\Delta\sigma_g$ value, most likely due to the

Table II. The Parameters Characterized the Dislocation Substructure in γ -Phase Grains

No.	Grain Type	Excess Dislocation Densities ρ_{\pm} , 10^{10}cm^{-2}	Internal Stresses, MPa	
			σ_{τ}	σ_l
1	grains with the mesh substructure	3.68	470	380
2	grains with plates of the first type ε -martensite	2.64	405	325
3	grains with plates of the second type ε -martensite	2.76	420	330
4	grains with strain microtwins	4.40	370	720

* $\rho < \rho_{\pm}$ indicates that the curvature-torsion of the γ -phase crystal lattice in grains with microtwins is elastic-plastic in nature.
 ** $\sigma_l = \sigma_l^{\text{plast}} + \sigma_l^{\text{elast}} = 370 + 350$ MPa indicates that the plastic component (370 MPa) of internal stresses is practically comparable to the elastic one (350 MPa), i.e., $\sigma_l^{\text{plast}} \approx \sigma_l^{\text{elast}}$.

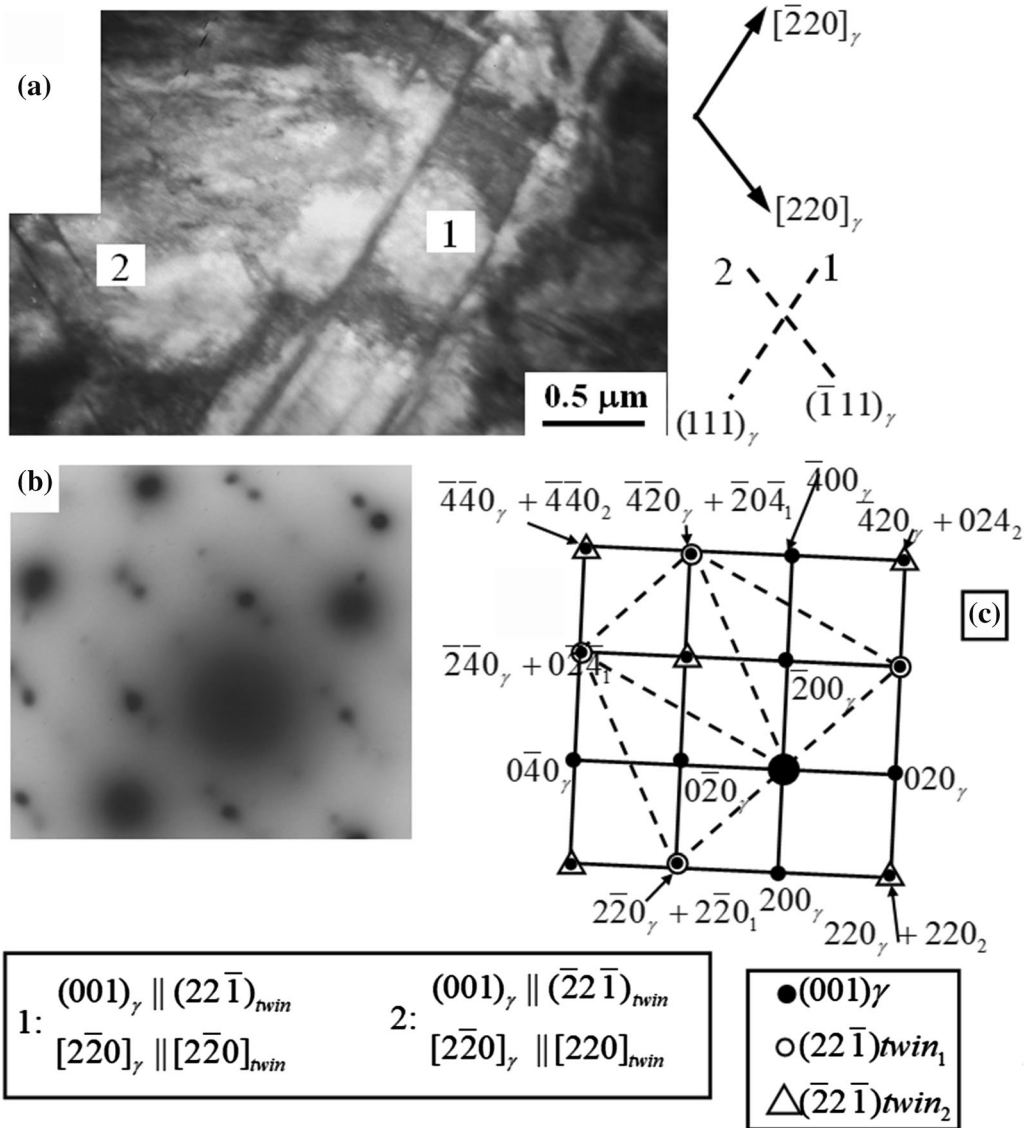


Fig. 10—The TEM image of a grain contained two systems of microtwins (1 and 2): (a)—bright field image; (b)—microdiffraction pattern; (c)—its indicated diagram.

softening mechanism upon changing the plate shape.^[53,54] As in most metals and alloys that were not prone to any transformations of the microstructure and phase composition under tensile loads, physical strain hardening took place simultaneously with this

phenomenon in the 304 steel samples. As a result, strains increased by $\Delta\sigma_{\text{ph}}$. These processes were characterized by two most probable variants. In the first case, the $\Delta\sigma_{\text{ph}} < \Delta\sigma_{\text{g}}$ relation was fulfilled. Therefore, physical strain hardening did not compensate for the

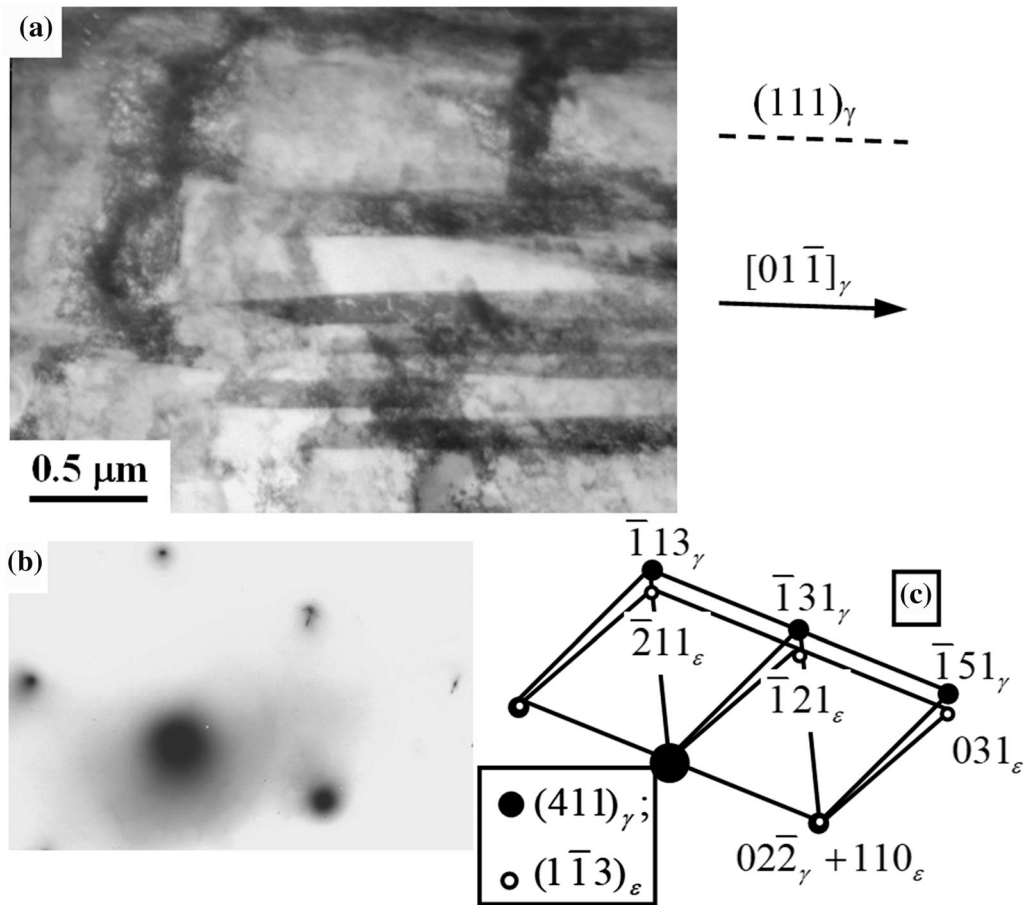


Fig. 11—TEM images of an austenite grain contained packets of microtwins and ϵ -martensite plates of in the weld metal: (a)—bright field image (dashed lines indicate the traces of the habit planes, the arrows show the segregation directions of packets of the ϵ -martensite plates in the γ -matrix indexes); (b)—microdiffraction pattern; (c)—its indicated diagram. The conditions for parallelism of the planes and directions between the γ -matrix and the ϵ -martensite plates are satisfied: $(411)_\gamma \parallel (1\bar{1}3)_\epsilon$ and $[01\bar{1}]_\gamma \parallel [110]_\epsilon$.

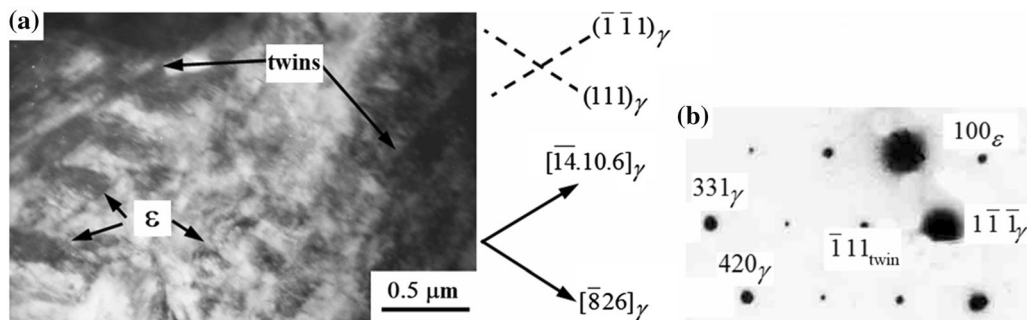


Fig. 12—TEM images of an austenite grain contained packets of microtwins and ϵ -martensite plates of in the weld metal: (a)—bright-field image; (b)—indicated microdiffraction pattern (contains reflections belonging to the $(12\bar{3})$ planes of the γ -phase, the $(\bar{2}\bar{3}1)$ package of microtwins and the (001) plates of ϵ -martensite). Near (a), the dashed lines show the habit plane indexes: for a package of microtwins is $(111)_\gamma$, for the ϵ -martensite plates is $(\bar{1}\bar{1}1)_\gamma$; arrows indicate indexes of the directions in the $(12\bar{3})$ plane of the γ -matrix: for microtwins is $[\bar{8}26]_\gamma$, for ϵ -martensite plates is $[\bar{4}.10.6]_\gamma$. The $(\bar{1}2\bar{3})_\gamma \parallel (001)_\epsilon$ and $(\bar{1}2\bar{3})_\gamma \parallel (\bar{2}\bar{3}1)_{\text{twin}}$ conditions are satisfied.

softening mechanism. In the second case, when the $\Delta\sigma_{\text{ph}} > \Delta\sigma_{\text{g}}$ relation was satisfied, the occurrence of local stress fluctuations due to material inhomogeneity was minimized by physical hardening and the deformation was uniform under the tensile load.^[55] For the studied 304 austenitic steel, two important factors had a significant effect on physical hardening. The first one

was associated with deformation-induced MT that caused relaxation of internal stresses.^[31,56–58] The second resulted in a significant level of solid solution hardening due to the dissolution of substitutional elements (nickel, chrome, molybdenum, manganese, titanium, and silicon), as well as carbon as an interstitial element in the FCC γ -phase. As a result, the competition

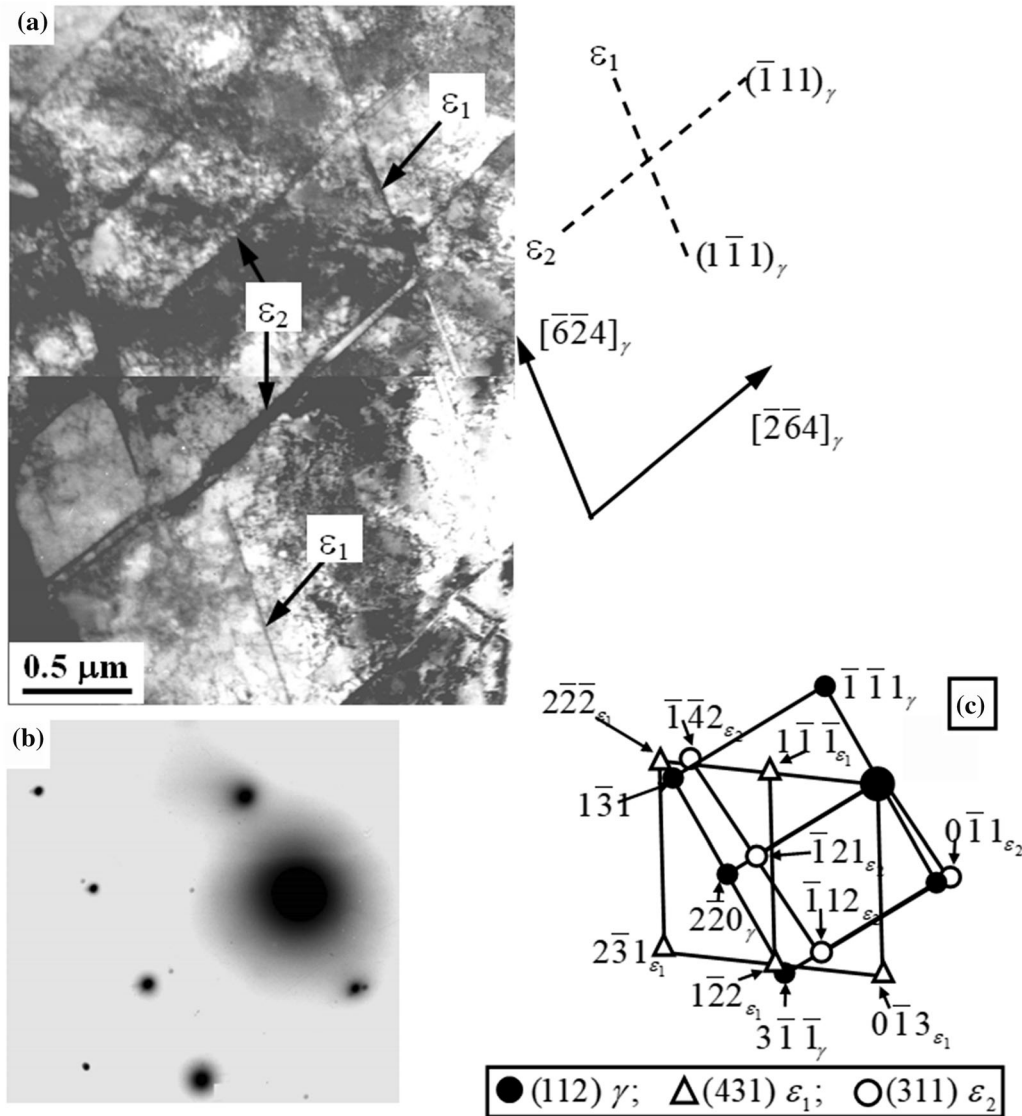


Fig. 13—TEM images of an austenite grain in the weld metal deformed to 5 pct: (a)—bright-field image (two ϵ_1 and ϵ_2) intersecting packets of the ϵ -martensite plates are highlighted; the dashed lines indicate the traces of the habit planes; the arrows show the segregation directions of the (ϵ_1 and ϵ_2) packets of the ϵ -martensite plates in the γ -matrix indexes); (b)—microdiffraction pattern; (c)—its indicated diagram. There are reflections related to the (112) planes of the ϵ -phase, as well as (431) and (311) planes ϵ -martensite.

of these factors was reflected in the $\sigma_{\text{true}} = f(\epsilon_{\text{true}})$ dependence (Figure 16(a)) and on the evolution of the strain field distributions on speckle images (Figures 17 and 18), showing the ϵ_{YY} longitudinal, ϵ_{XX} transverse and ϵ_{XY} shear strains on the sample surfaces at different stress levels.

In the elastic stage, a fragmented structure was observed in the strain field distributions on the as-received sample surface (Figure 17, images 1 (ϵ_{YY}), 1 (ϵ_{XX}), and 1 (ϵ_{XY})). This fragmentation was characterized by many local tensile strain peaks ($\epsilon_{YY} > 0$) in the ϵ_{YY} longitudinal direction, but compressive ones ($\epsilon_{XX} < 0$) in the ϵ_{XX} transverse direction (Figure 17, images 1 (ϵ_{YY}) and 1 (ϵ_{XX})). Small local strain peaks of different signs ($\epsilon_{XY} > 0$ or $\epsilon_{XY} < 0$) were found in the ϵ_{XY} shear strain distribution (Figure 17, image 1 (ϵ_{XY})).

These small local strain peaks included entire groups of grains at the macro level.

Transition from the elastic stage to the plastic strain one (Figure 16(a), curve A, points 1 and 2) was reflected by the merging of small local strain zones into larger regions (Figure 17, images 2 (ϵ_{YY}) and 2 (ϵ_{XX})). A further increase in applied stresses caused a change in the as-received sample shape. Its width reduced in the central part with the formation of a 'neck' (Figure 17, images 3 (ϵ_{YY})–5 (ϵ_{YY}), 3 (ϵ_{XX})–5 (ϵ_{XX})). As a result, there was a tendency to 'contraction' of the local strain zones into single large area in the central part of the sample with a significant increase in plastic strains inside. In this area, initially, the ϵ_{YY} plastic strain level was by 1.5 times greater than average values over the entire sample surface (Figure 17, image 4 (ϵ_{YY})), but this ratio enhanced up to 2.5 (Figure 17, image 5 (ϵ_{YY})) at

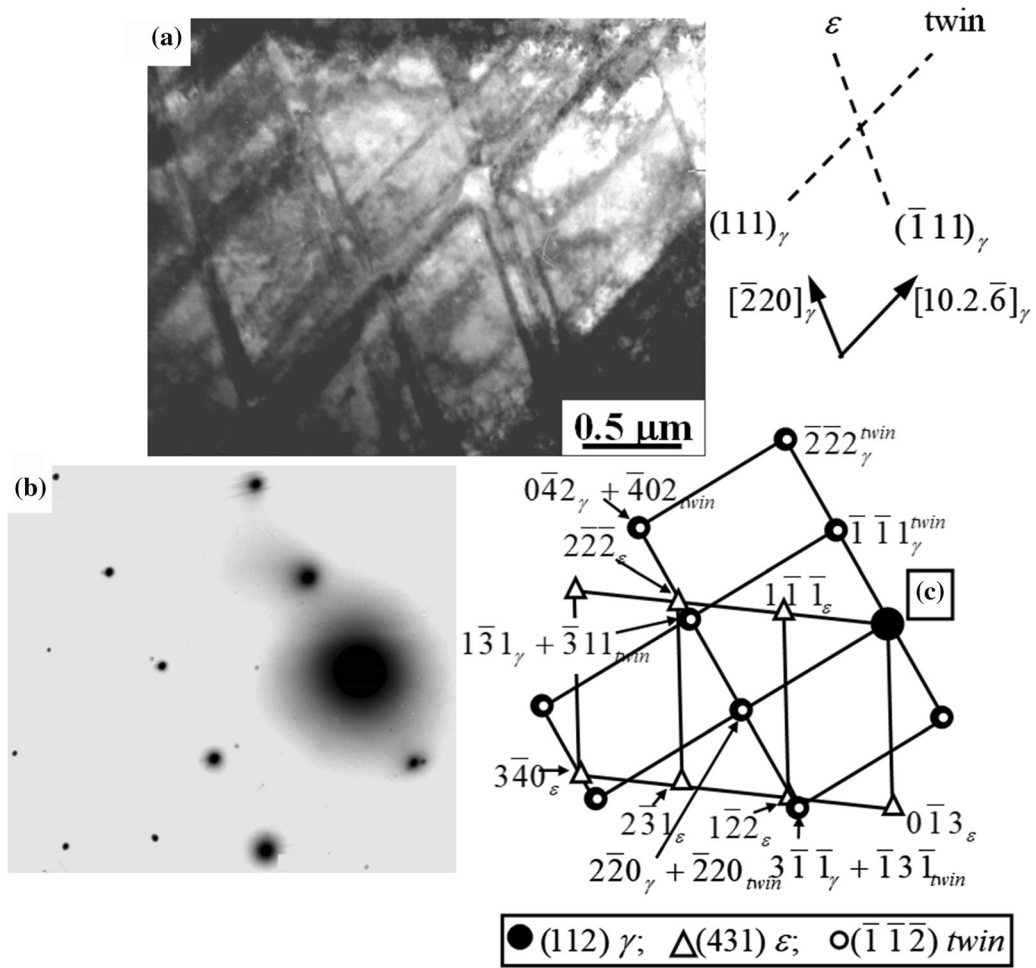


Fig. 14—TEM images of an austenite grain in the weld metal deformed up to 5 pct: (a)—intersecting packets of microtwins and the ϵ -martensite plates; the dashed lines indicate the traces of the habit planes (the arrows show the segregation directions of the packets of microtwins and the ϵ -martensite plates in the γ -matrix indexes); (b)—microdiffraction pattern; (c)—its indicated segregation diagram. The conditions for parallelism of the planes and the directions between the γ -matrix, the packets of microtwins and the ϵ -martensite plates are satisfied: $(112)_\gamma \parallel (\bar{1}\bar{1}\bar{2})^{twin}$, $[\bar{2}20]_\gamma \parallel [\bar{2}20]^{twin}$, $(112)_\gamma \parallel (431)_\epsilon$, and $[3\bar{1}\bar{1}]_\gamma \parallel [1\bar{2}2]_\epsilon$.

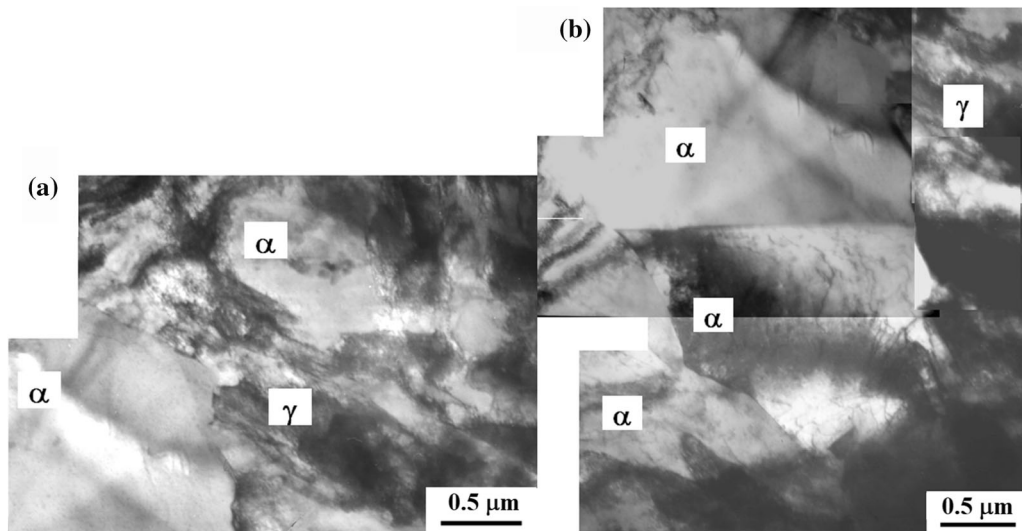


Fig. 15—TEM images of the weld metal deformed up to 37 pct: (a)— α -martensite grains located along the austenite grain boundaries; (b)—groups of α -martensite grains (α —the α -martensite grains; γ —the austenite grains).

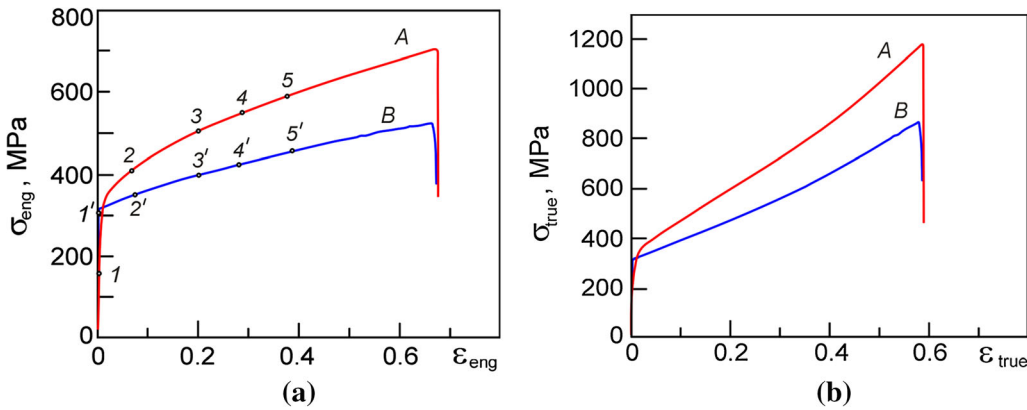


Fig. 16—Engineering (a) and true (b) stress–strain curves under uniaxial tensile load (*A*—the as-received sample; *B*—the welded sample). Points 1 to 5 on curve *A* and 1' to 5' on curve *B* mark states for which the speckle images of strain field distributions are shown in Figs. 17 and 18, respectively.

the final stage (Figure 16, curve *A*, point 5). This phenomenon correlated well with changes in the strain field distributions in the ε_{XX} transverse direction in the central part of the sample during the ‘neck’ formation (Figure 17, image 5 (ε_{XX})).

In contrast to the strain field distributions in both ε_{YY} longitudinal and ε_{XX} transverse directions, described above, the lateral faces of the as-received sample were stress raisers for the ε_{XY} shear strains (Figure 17, image 3 (ε_{XY})–4 (ε_{XY})). At the final stage (Figure 16(a), curve *A*, transition from point 4 to 5), a layered structure of longitudinally elongated strain peaks was found in the ‘neck’ region (Figure 17, image 5 (ε_{XY})).

Such strain field evolution patterns were due to the changes in the microstructure and phase composition under tensile stresses. These data were confirmed in the first part of the paper on the basis of the results of the TEM studies.

For the welded samples, a fragmented structure was observed in the form of local macroregions at the elastic stage (Figure 16, point 1'). Within these macroregions, strain levels differed by $\pm(30\text{--}40)$ pct from the average one over the entire area of the welded sample surface (Figure 18, image 1 (ε_{YY})). In the macroregions, strains were elastic and varied from 0.11 up to 0.31 pct in the ε_{YY} longitudinal direction. In the ε_{XX} transverse direction, these variations were within the range from 0.01 to 0.15 pct (Figure 18, image 1 (ε_{XX})), but ε_{XY} shear strains differed by 0.04–0.06 pct (Figure 18, image 1 (ε_{XY})). According to generally accepted concepts,^[57] these local macroregions were a kind of deformation or elastic-plastic domains, which could include some groups of grains. The lateral faces of the welded sample were stress concentrators and characterized by plastic strain peaks consisted of these domains. In addition, dislocation slips were observed in grains with the most favorable orientation relative to the direction of the applied stress at its lower values.^[57–59] Also, deformation-induced MT had occurred in local areas of the welded sample, which contributed to stress relaxation. As a result, strains had been developed very inhomogeneously that caused the formation of these fragmentary and uneven domains on the sample surface. The number of large ones along the

surface was low, but small domains were grouped into local blocks (Figure 18, images 1 (ε_{YY}), 1 (ε_{XX}), 1 (ε_{XY})).

It should be noted that elastic-plastic domains, arranged in a quasi-periodic manner and elongated perpendicular to the tensile axis, corresponded to the elastic strain region on both curves *A* and *B* in Figure 16. As is known, the formation of local plastic strain centers was firstly initiated at the microlevel in the WM and HAZ regions at the elastic stage, then developed at the mesolevel with increasing stresses, and finally formed at the macrolevel.^[34] It was the response of the steel to this effect, which was recorded on the presented speckle images at the macrolevel and correlated with the curve dynamics in both $\sigma_{\text{eng}}-\varepsilon_{\text{eng}}$ and $\sigma_{\text{true}}-\varepsilon_{\text{true}}$ coordinates (Figure 16).

The transition from the elastic strain region to the plastic one (Figure 16, from point 1' to 2') caused a change in all strain field distributions on the welded sample surface (Figure 18, images 2 (ε_{YY}), 2 (ε_{XX}) and 2 (ε_{XY})). Small local areas merged into large homogeneous regions characterized by high strain levels. In this case, a local macroregion with lower plastic strain levels (compared to the average one over the entire surface) was in the WM region and in the central part on the sample left side according to the ε_{YY} longitudinal and ε_{XX} transverse strain distributions. Also, local microregions with the same strain values were in the lower grip area (Figure 18, image 2 (ε_{YY})). These low strain levels in the mentioned areas were indicative of the higher strength properties of the steel at these locations.

The local macroregion in the central part of the sample was due to the presence of the welded joint. Uneven heating of the steel had caused residual stresses that had changed the WM and HAZ elastic moduli.^[60] Consequently, this prevented the material from deformations in accordance with the Poisson effect under external loads. The elastic modulus had changed unevenly in accordance with the thermal cycle of each microvolume in the WM and HAZ regions. Accordingly, compressive and tensile residual stresses alternated in this area.^[60] As a result, this metal unevenness resulted in the formation of local regions characterized

by conditions that contributed to MT, but this process had been blocked in other steel microvolumes (Figure 18). It should be noted that deformation-induced MT were determined by the microstructural studies for both samples and described above. In this case, it was necessary to consider the non-uniform distribution of residual stresses in the WM region.^[61]

Fig. 18—The speckle images of the ϵ_{YY} longitudinal, ϵ_{XX} transverse and ϵ_{XY} shear strain distributions on the welded sample surface corresponding to the points on curve *B* in Fig. 16: 1'— $\epsilon_{eng} = 0.36$ pct; 2'— $\epsilon_{eng} = 8.63$ pct; 3'— $\epsilon_{eng} = 20.30$ pct; 4'— $\epsilon_{eng} = 28.98$ pct; 5'— $\epsilon_{eng} = 38.70$ pct.

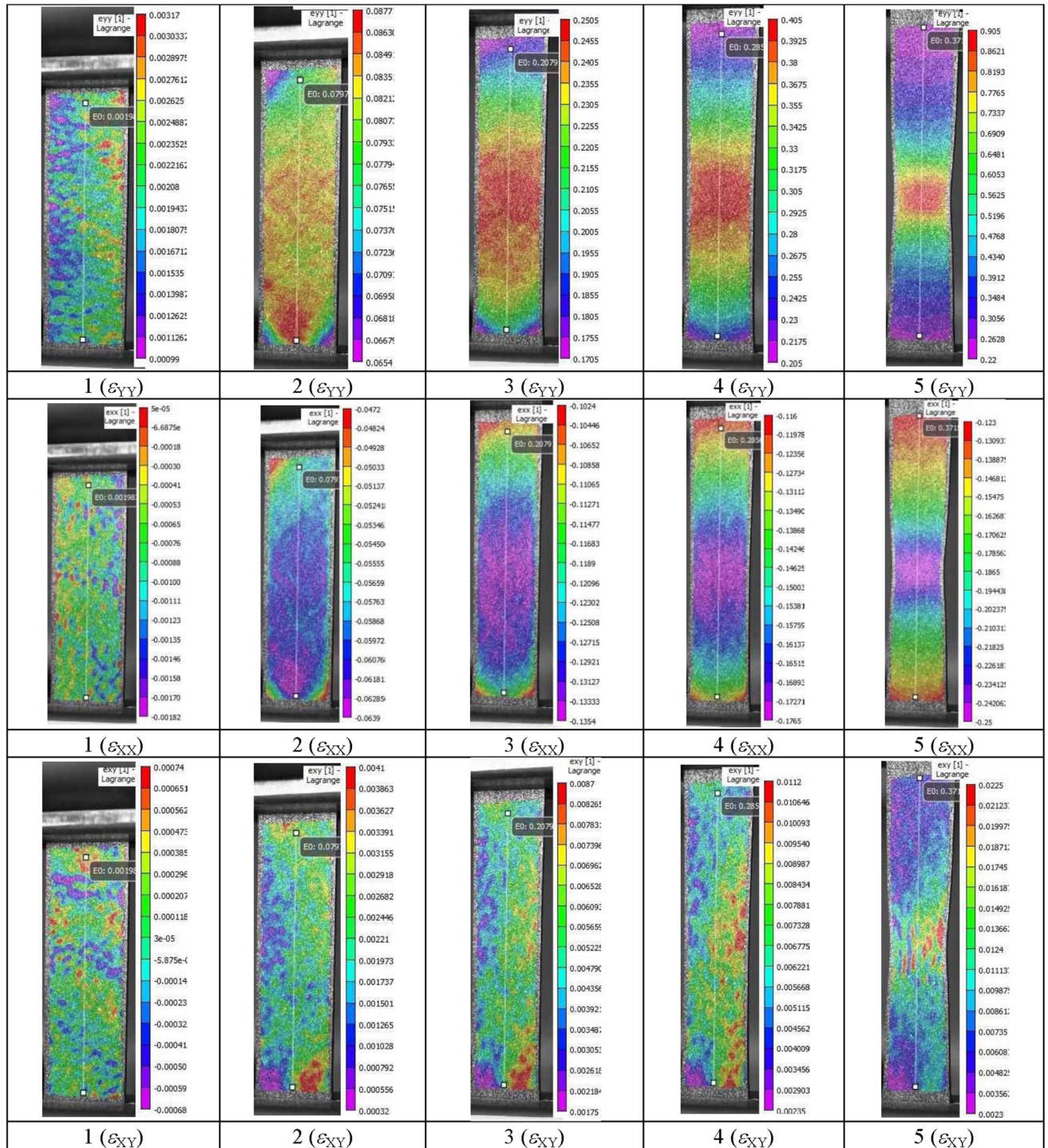
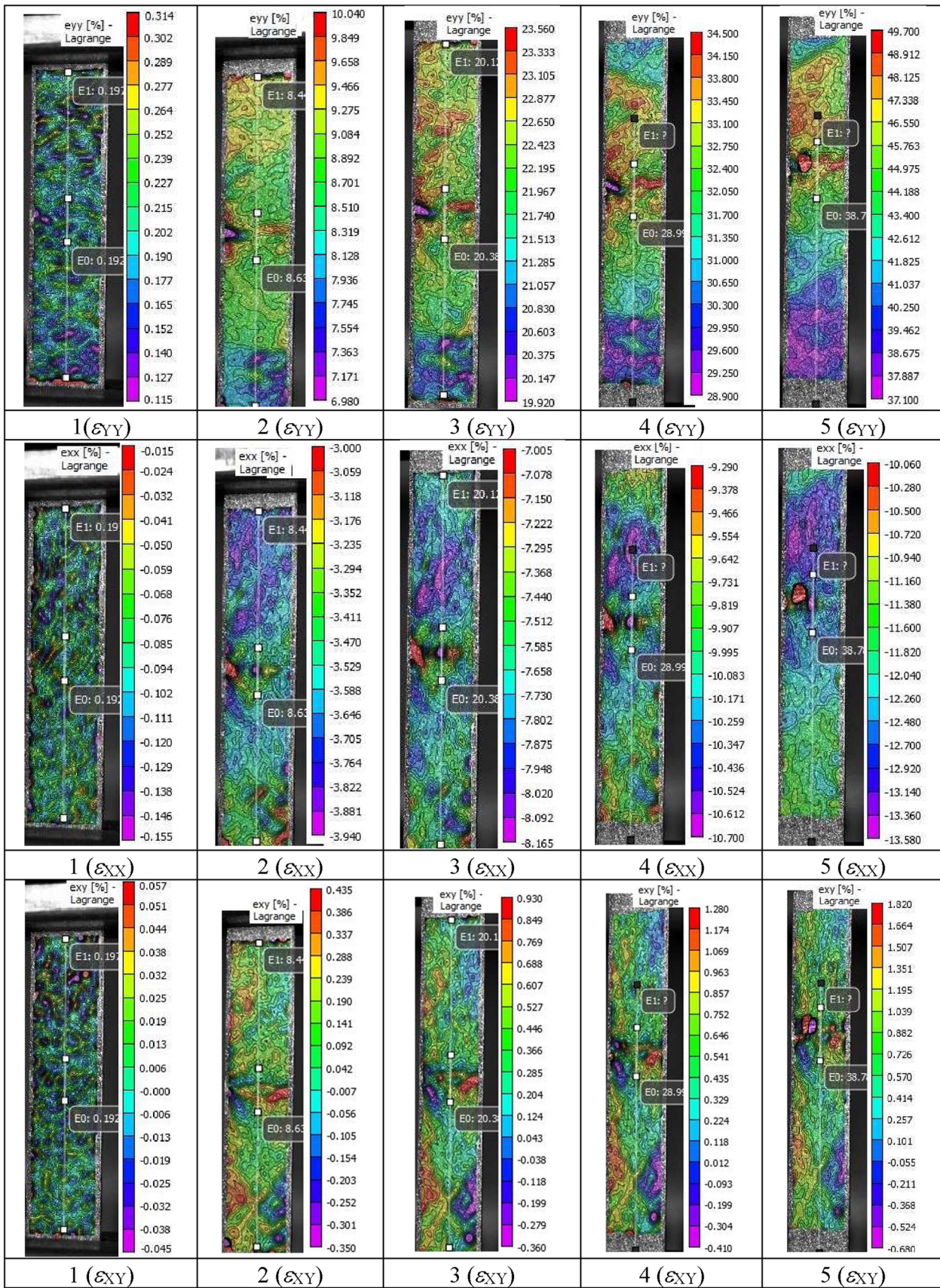


Fig. 17—The speckle images of the ϵ_{YY} longitudinal, ϵ_{XX} transverse and ϵ_{XY} shear strain distributions on the as-received sample surface corresponding to the points on curve *A* in Fig. 16: 1— $\epsilon_{eng} = 0.19$ pct; 2— $\epsilon_{eng} = 7.97$ pct; 3— $\epsilon_{eng} = 20.79$ pct; 4— $\epsilon_{eng} = 28.90$ pct; 5— $\epsilon_{eng} = 37.10$ pct.



The authors of this paper experimentally showed the uneven distribution of residual stresses in the WM region of the 0.09 pct C-0.8 pct Si-1.5 pct Mn structural steel. At the same time, it was found that compressive and tensile stresses were both in the longitudinal and transverse directions relative to the weld axis. These data were correlated with the speckle images presented in Figure 18.

As external stresses increased on the right-side face in the central part of the welded joint (a mirror image of its left-face), a local peak of plastic stains was observed that possessed a higher stain levels than in neighboring local areas (Figure 18, images 3 (ϵ_{YY})–5 (ϵ_{YY})). This fact indicated that deformation-induced MT had occurred in the local region, which resulted in activation of the martensitic deformation mechanism that caused relaxation of internal stresses in these local areas. Also, an additional uneven distribution of post-weld residual stresses was observed in the WM region (Figure 18, images 2 (ϵ_{XX})–5 (ϵ_{XX}) and 2 (ϵ_{XY})–5 (ϵ_{XY})). Thus, the shown changes in the strain field distributions reflected the presence of stress concentrators. Respectively, deformation-induced $\gamma \rightarrow \alpha \rightarrow \epsilon$ MT had occurred in this part of the welded sample under conditions of the non-uniform distribution of residual stresses.

Finally, it should be noted that quite a lot of attention had already been paid to the study of the processes of evolution of the microstructure and mechanical properties of the metastable austenitic steels upon deformation by various methods.^[54,62,63] In particular, it was shown that patterns of formation of the microstructure and phase composition were greatly determined by the degree, type, and mode of deformation. All these features were manifested in a wide range of microstructural transformations during plastic deformation of the metastable austenitic steels.^[31,64] Some authors discussed similar $\gamma \rightarrow$ twins $\rightarrow \epsilon \rightarrow \alpha$ transformations,^[64–66] but the statements were based on the results of X-ray structural analysis, as well as optical and electron microscopy in most cases.^[67–69] So far, little extensive data on the effect of deformation on the $\gamma \rightarrow$ twins $\rightarrow \epsilon \rightarrow \alpha$ transformations in the weld metal and HAZ data were published for this grade of steels. It should also be noted that X-ray structural analysis was mainly applied for this purpose. Thus, the authors of Reference 70 showed that a rearrangement of the crystal lattice was observed in the weld region and the subsequent deformation accelerated this process.^[71] The above brief analysis of the previously published papers enabled to conclude that this detailed TEM investigation of the welded joint subjected to plastic deformation expanded understanding of the changes in its microstructure and phase composition. This is especially true since the presented data were obtained on the basis of indisputable evidence of the crystal lattice rearrangement using the orientation relations and theoretically calculated electron diffraction patterns, as well as comparing them with the TEM images. In addition, these patterns were connected with both stress–strain curves and strain field distributions.

IV. CONCLUSIONS

Based on the obtained results, the following conclusions can be drawn:

1. The results of the transmission electron microscopic studies showed that the significant effect of plastic strains had been on the microstructure and phase composition of the 304 austenitic stainless, including the weld metal and heat affected zone. After strain up to 37 pct, the deformation-induced $\gamma \rightarrow \alpha$ transformation was observed in addition to the $\gamma \rightarrow \epsilon$ one. The elastic-plastic bending-torsion had occurred in the α -martensite crystal lattice, while it had been only plastic in the γ -phase austenite grains (σ_1 was 340 MPa, but σ_τ was 400 MPa).
2. The studied deformation of the welded sample caused the formation of ϵ -martensite in both weld and base metals. After strain to $\epsilon_{\text{eng}} = 25$ pct, the weld metal microstructure represented only by γ -phase grains with mechanical microtwins and ϵ -martensite plates. The $\rho > \rho_\pm$ and $\sigma_1 > \sigma_\tau$ conditions were fulfilled in all γ -phase grains. Accordingly, bending-torsion of the γ -phase crystal lattice had the plastic character. In the γ -phase grains with mechanical microtwins, the $\rho < \rho_\pm$ and $\sigma_1 < \sigma_\tau$ conditions were satisfied and bending-torsion of the γ -phase crystal lattice was characterized by the elastic-plastic manner. This could cause the formation of microcracks. If the density of the γ -phase grains with microtwins was not high, all possible microcrack unlikely transformed into macro- ones. As a result, plastic deformation of the welded joint resulted in the significant elastic-plastic distortion of the γ -phase crystal lattice only in the base metal (without its fracture).
3. Based on the analysis of the stress–strain curves under uniaxial tension, high plasticity and significant strain hardening of the 304 steel were established. The presence of the welded joint reduced the ratio of ultimate tensile strength to the yield point from 3.3 down to 2.6.
4. At the elastic stage, a fragmented structure was observed in the form of local macroregions, within which strain levels differed by $\pm(30\text{--}40)$ pct from the average one over the entire area of the welded sample surface. In these local macroregions, strains were elastic and varied from 0.11 up to 0.31 pct in the longitudinal direction. In the transverse direction, these variations were within the range from 0.01 to 0.15 pct, but shear stains differed by 0.04–0.06 pct. These local macroregions were a kind of deformation or elastic-plastic domains, which could include some groups of grains. The lateral faces of the welded sample were stress concentrators and characterized by plastic strain peaks consisted of these domains.
5. The transition from the elastic strain region to the plastic one caused the change in all strain field distributions on the welded sample surface. Small local areas merged into large homogeneous regions characterized by high strain levels.

- The presence of the welded joint resulted in the formation of local macroregions with both lower and higher plastic strain levels on the longitudinal and transverse field distributions in the speckle images than the averaged values over the entire sample surface. These macroregions was due to the inhomogeneity of residual stresses and the deformation-induced $\gamma \rightarrow \alpha \rightarrow \varepsilon$ martensitic transformations.

FUNDING

The work was carried out within the framework of the state assignment of the Ministry of Science and Higher Education of the Russian Federation (Project No. FEMN-2020-0004).

CONFLICT OF INTEREST

The authors declare that they have no conflict of interest.

REFERENCES

- M. Soleimani, A. Kalhor, and H. Mirzadeh: *Mater. Sci. Eng. A.*, 2020, vol. 795, p. 140023.
- F. Borgioli: *Metals.*, 2020, vol. 10(2), p. 187.
- L. Gardner: *Thin-Walled Struct.*, 2019, vol. 141, pp. 208–16.
- M.H. Hebdon and J.T. Provinces: *J. Perform. Constr. Facil.*, 2020, vol. 34(6), p. 04020108.
- G. Kim, T. Kim, B. Hwang, and J. Kim: *Thin-Walled Struct.*, 2020, vol. 155, p. 106950.
- H.X. Yuan, J.D. Gao, M. Theofanous, L. Yang, and B.W. Schafer: *J. Constr. Steel Res.*, 2020, vol. 173, p. 106239.
- E. Folkhard: *Welding Metallurgy of Stainless Steels*, Springer, New York, 1984.
- J.C. Lippold and D.J. Kotecki: *Welding Metallurgy and Weldability of Stainless Steels*, Wiley, New Jersey, 2005.
- M. Muhammed, M. Mustapha, T.L. Ginta, A.M. Ali, F. Mustapha, and C.C. Hampo: *Processes.*, 2020, vol. 8(7), p. 811.
- K. Pańcikiewicz, A. Świerczyńska, P. Hućko, and M. Tumida-jewicz: *Materials.*, 2020, vol. 13(20), p. 4540.
- G. Rogalski, A. Świerczyńska, M. Landowski, and D. Fydrich: *Metals.*, 2020, vol. 10(5), p. 559.
- Q. Wang, J. Shen, S. Hu, G. Zhao, and J. Zhou: *Materials.*, 2020, vol. 13(18), p. 4016.
- A. Saboori, A. Aversa, G. Marchese, S. Biamino, M. Lombardi, and P. Fino: *Appl. Sci.*, 2020, vol. 10(9), p. 3310.
- W. Jin, C. Zhang, S. Jin, Y. Tian, D. Wellmann, and W. Liu: *Appl. Sci.*, 2020, vol. 10(5), p. 1563.
- N. Haghdadi, M. Laleh, M. Moyle, and S. Primig: *J. Mater. Sci.*, 2021, vol. 56, pp. 64–107.
- A. Gupta, A. Kumar, T. Baskaran, S.B. Arya, and R.K. Khartikar: *Trans. Indian Inst. Met.*, 2018, vol. 71(7), pp. 1595–606.
- V. Hosseini, K. Hurtig, and L. Karlsson: *Weld. World.*, 2020, vol. 64(4), pp. 283–99.
- G.-G. Youn, Y.-J. Kim, and Y. Miura: *Nucl. Eng. Technol.*, 2021, vol. 53(4), pp. 1357–68.
- A. O'Brien: *Welding Handbook*, 9th ed., vol. 2, *Welding Processes*, Part 1. American Welding Society, Miami, 2004.
- A. O'Brien: *Welding Handbook*, 9th ed., vol. 3, *Welding Processes*, Part 2. American Welding Society, Miami, 2007.
- D. Radaj: *Heat Effects of Welding. Temperature Field, Residual Stress, Distortion*, Springer, Berlin, 1992.
- E. Niemi: *Stress Determination for Fatigue Analysis of Welded Components*, Abington Publishing, Cambridge, 1995.
- Z. Feng: *Processes and Mechanisms of Welding Residual Stress and Distortion*, Woodhead Publishing, Cambridge, 2005.
- G.M. Hassan: *Opt. Lasers Eng.*, 2021, p. 137106394.
- M.I. Latypov, J.-C. Stinville, J.R. Mayeur, J.M. Hestroffer, T.M. Pollock, and I.J. Beyerlein: *Scripta Mater.*, 2021, vol. 192, pp. 78–82.
- W. Zhang, Y. Xie, L. Peng, H. Liao, and Y. Wan: *J. Nucl. Mater.*, 2021, vol. 543, p. 152565.
- J. Hensel, T. Nitschke-Pagel, D. TchoffoNgoula, H.-T. Beier, D. Tchuindjang, and U. Zerbst: *Eng. Fract. Mech.*, 2018, vol. 198, pp. 123–41.
- L. Pan, B.P. Athreya, J.A. Forck, W. Huang, L. Zhang, T. Hong, W. Li, W. Ulrich, and J.C. Mach: *Weld. World.*, 2013, vol. 57, pp. 685–91.
- M. Odnobokova, A. Belyakov, and R. Kaibyshev: *Adv. Eng. Mater.*, 2015, vol. 17(12), pp. 1812–20.
- Z. Yanushkevich, A. Lugovskaya, A. Belyakov, and R. Kaibyshev: *Mater. Sci. Eng., A.*, 2016, vol. 667, pp. 279–85.
- M. Odnobokova, A. Belyakov, and R. Kaibyshev: *Mater. Sci. Forum.*, 2017, vol. 879, pp. 1414–9.
- B.-A. Behrens, S. Hübner, A. Bouguecha, J. Knigge, K. Voges-Schwieger, and K. Weilandt: *Adv. Mater. Res.*, 2010, vol. 137, pp. 1–33.
- V.V. Mishakin, V.A. Klyushnikov, and A.V. Gonchar: *Techn. Phys.*, 2015, vol. 60(5), pp. 665–8.
- S.V. Panin, V.L. Klimenov, O.N. Nekhoroshkov, and V.E. Panin: *Phys. Mesomech.*, 2001, vol. 4(2), pp. 51–64. (in Russian).
- A.N. Smirnov, N.A. Popova, N.V. Ababkov, E.L. Nikonenko, E.A. Ozhiganov, and N.A. Koneva: *Fundam. Probl. Mod. Mater. Sci.*, 2018, vol. 15(3), pp. 434–41. (in Russian).
- N.A. Popova, A.N. Smirnov, E.L. Nikonenko, N.V. Ababkov, and N.A. Koneva: *Proc. Univ. Phys.*, 2019, vol. 62(9), pp. 48–57. (in Russian).
- Specification on the CL-11 Electrodes. <https://www.spetsselectrode.ru/electrod/cl11.htm>. Accessed 28 October 2021.
- ISO 3581:2016 *Welding Consumables—Covered Electrodes for Manual Metal Arc Welding of Stainless and Heat-Resisting Steels—Classification*.
- ISO/DIS 3651-2:1998 *Determination of Resistance to Intergranular Corrosion of Stainless Steels—Part 2: Ferritic, Austenitic and Ferritic-Austenitic (Duplex) Stainless Steels—Corrosion Test in Media Containing Sulfuric Acid*.
- M.A. Sutton, J.-J. Orteu, and H.W. Schreier: *Image Correlation for Shape, Motion and Deformation Measurements. Basic Concepts, Theory and Applications*, Springer, Boston, 2009.
- R. Bobbili and V. Madhu: *J. Alloy. Compd.*, 2016, vol. 684, pp. 162–70.
- P.B. Hirsch, A. Howrie, R.B. Nicholson, D.W. Pashley, and M.J. Whelan: *Electron Microscopy of Thin Crystals*, Butterworths, London, 1965.
- N.A. Koneva and E.V. Kozlov: *Sov. Phys. J.*, 1991, vol. 34, pp. 224–36.
- N.A. Koneva, E.V. Kozlov: *Perspective Materials*. TSU Publishing House, Tula, 2006. pp. 267–320. (in Russian).
- B.N. Strunin: *FTT.*, 1967, vol. 9(3), pp. 805–12. (in Russian).
- N.A. Koneva and E.V. Kozlov: *Proc. Univ. Phys.*, 1982, vol. 8, pp. 3–14. (in Russian).
- L.I. Lysak, B.I. Nikolin: *Physical Foundations of Heat Treatment of Steel*. Technics, Kiev, 1975. (in Russian).
- O.O. Lambakhar and Y.I. Pascal: *Proc. Univ. Phys.*, 1977, vol. 1, pp. 158–61. (in Russian).
- T.F. Volynova: *High Manganese Steels and Alloys*, Metallurgy, Moscow, 1988. (in Russian).
- L.M. Utevsky: *Diffraction Electron Microscopy in Metal Science*, Metallurgy, Moscow, 1973. (in Russian).
- N. Koneva, S. Kiseleva, and N. Popova: *Structure Evolution and Internal Stress Fields. Austenitic Steel*, LAP LAMBER Academic Publishing, Saarbrücken, 2017. (in Russian).
- O.P. Maksimkin and M.N. Gusev: *Phys. Met. Met. Sci.*, 2010, vol. 110(5), pp. 524–9. (in Russian).
- V.A. Starenchenko, Y.D. Lipatnikova, and Y.V. Solovyova: *Proc. Univ. Phys.*, 2018, vol. 61(4), pp. 106–14. (in Russian).

54. S.V. Dobatkin, O.V. Rybalchenko, N.A. Enikeev, A.A. Tokar, and M.M. Abramova: *Mater. Lett.*, 2016, vol. 166, pp. 276–9.
55. G.A. Salishchev, R.G. Zariipova, and A.A. Zakirova: *Met. Sci. Heat Treat.*, 2006, vol. 48, pp. 70–5.
56. M. Tikhonova, N. Enikeev, R. Valiev, A. Belyakov, and R. Kaibyshev: *Mater. Sci. Forum.*, 2016, vol. 838–9, pp. 398–403.
57. V.L. Romanova, R.P. Balakhonov, L.V. Panin, E.E. Batukhtina, M.S. Kazachenok, and B.C. Shakhidzhanov: *Phys. Mesomech.*, 2017, vol. 20(3), pp. 81–90. (in Russian).
58. T.V. Muravyov and L.B. Zuev: *J. Techn. Phys.*, 2008, vol. 78(8), pp. 137–42. (in Russian).
59. N.A. Koneva, E.V. Kozlov: *Structural Levels of Plastic Deformation and Fracture*. Science, Novosibirsk, 1990. pp. 123–86. (in Russian).
60. S. Yoshida, T. Sasaki, M. Usui, and I.-K. Park: *Phys. Mesomech.*, 2015, vol. 18(6), pp. 32–44.
61. Y.N. Saraev, N.I. Golikov, V.V. Dmitriev, I.I. Sannikov, V.P. Bezborodov, and A.A. Grigorieva: *MetalProcess.*, 2013, vol. 3, pp. 16–24. (in Russian).
62. Y.N. Goikhenberg: *Met. Sci. Heat Treat.*, 2015, vol. 56, pp. 477–82.
63. Y.B. Das, A.N. Forsey, T.H. Simm, K.M. Perkins, M.E. Fitzpatrick, S. Gungor, and R.J. Moat: *Mater. Des.*, 2016, vol. 112, pp. 107–16.
64. M. Okayasu and S. Tomida: *Mater. Sci. Eng. A.*, 2017, vol. 684, pp. 712–25.
65. I.Y. Litovchenko, S.A. Akkuzin, N.A. Polekhina, A.N. Tyumentsev, and E.P. Naiden: *Russ. Phys. J.*, 2016, vol. 59, pp. 782–7.
66. Z.H. Cai, H. Ding, Z.Y. Tang, and R.D.K. Misra: *Mater. Sci. Eng. A.*, 2016, vol. 676, pp. 289–93.
67. E.G. Astafurova and Y.I. Chumlyakov: *Phys. Met. Metallogr.*, 2009, vol. 108, p. 510.
68. E.G. Astafurova, G.G. Maier, E.V. Melnikov, V.A. Moskvina, V.F. Vojtsik, G.N. Zakharov, A.I. Smirnov, and V.A. Bataev: *Phys. Mesomech.*, 2018, vol. 21, pp. 263–73.
69. I.A. Kurzina, A.I. Potekaev, N.A. Popova, E.L. Nikonenko, T.V. Dement, A.A. Klopotov, V.V. Kulagina, and V.A. Klimenov: *Russ. Phys. J.*, 2018, vol. 61, pp. 715–21.
70. V.A. Klimenov, S.F. Gnyusov, A.I. Potekaev, A.A. Klopotov, Y.A. Abzaev, K.A. Kurgan, M.R. Marzol, S.V. Galsanov, V.Y. Tsellermayer, and E.S. Marchenko: *Russ. Phys. J.*, 2017, vol. 60, pp. 990–1000.
71. N.A. Popova, A.N. Smirnov, E.L. Nikonenko, N.V. Ababkov, and N.A. Koneva: *Russ. Phys. J.*, 2020, vol. 62, pp. 1587–94.

Publisher's Note Springer Nature remains neutral with regard to jurisdictional claims in published maps and institutional affiliations.